University of Birmingham

A reflection on analytical tornado-like vortex flow field models

Gillmeier, Stefanie; Sterling, Mark; Hemida, Hassan; Baker, Christopher

[Link to publication on Research at Birmingham portal](#)

A reflection on analytical tornado-like vortex flow field models

S. Gillmeier[1], M. Sterling[2], H. Hemida[3], C.J. Baker[4]

Department of Civil Engineering, School of Engineering, University of Birmingham, Edgbaston, Birmingham, B15 2TT, United Kingdom, [1]stefaniegillmeier-wls@web.de, [2]m.sterling@bham.ac.uk, [3]h.hemida@bham.ac.uk, [4]c.j.baker@bham.ac.uk

Abstract

Given the difficulties associated with undertaking full-scale measurements in tornadoes, recourse is often made to models. In this field, analytical models have, perhaps surprisingly, stood the test of time, with the Rankine, Burgers-Rott and Sullivan models frequently invoked to model the flow field of a tornado. These mathematical models are by their very nature, a simplification of what is a highly complex phenomenon. However, in many cases they have been represented as the 'truth' without the fundamental assumptions governing the model being either explored in detail or even acknowledged. This paper attempts to rectify this by giving detailed information about assumptions and limitations of each vortex model and critically assesses the ability (or otherwise) of the Rankine, Burgers-Rott, Sullivan, and the recently published Baker vortex model to simulate tornado-like flow. Comparisons are made to the flow field of a physically simulated tornado, which by its very nature is also a model, but arguably more realistic.

It was found that the vortex models are able to represent certain flow patterns at certain heights but fail, due to their simplifications, in replicating the entire three-dimensional flow structure obtained experimentally.

Keywords: Laboratory simulated tornado vortex; Analytical vortex models; Rankine vortex; Burgers-Rott vortex; Sullivan vortex; Baker vortex

1. Introduction

Within the Wind Engineering community, increasing attention is being paid to the effects of non-stationary, non-synoptic winds, i.e. tornadoes. The structure of full-scale tornadoes is highly complex, showing a three-dimensional flow field, instabilities, singularities and non-linear effects (e.g. Lewellen, 1993; Davies-Jones et al., 2001; Alexander and Wurman, 2008; Karstens et al., 2010). In order to understand the physical processes present in a tornado flow field, simplified models are needed, which reduce the degree of freedom present in full-scale observations, and therefore allow a detailed and statistically representative evaluation of velocity and pressure fields. In order to provide this type of datasets, the tornado-like flow field was modelled experimentally

40 and/or numerically by several authors such as Ward, 1972; Church et al., 1979; Lewellen et al.,
41 1997; Haan et al., 2008; Mishra et al., 2008; Natarajan, 2011; Sabareesh et al., 2012; Refan et al.,
42 2014; Gillmeier et al., 2016; Liu and Ishihara, 2016; Nolan et al., 2017 and Tang et al., 2017. An
43 attempt to analytically model the three-dimensional flow in the boundary layer of a tornado-like
44 vortex was made by Kuo (1971) by alternatingly solving the two nonlinear boundary-layer
45 equations for the radial and vertical distribution of velocities. The Bloor and Ingham vortex model
46 (1987) and the Vyas-Majdalani vortex model (Vyas et al., 2003) are exact inviscid solutions to the
47 Euler's equations in a confined conical and cylindrical domain, respectively. Xu and Hangan
48 (2009) analytically modelled an inviscid tornado-like vortex using a free narrow jet solution
49 combined with a modified Rankine vortex. However, it needs to be mentioned here that this
50 combined model is not an exact solution to the Navier-Stokes-Equations. Wood and White (2011)
51 presented a new parametric model of vortex tangential-wind profiles, which is based on the
52 Vatistas model (Vatistas et al., 1991) and is primarily designed to depict realistic-looking
53 tangential wind profiles observed in atmospheric vortices.
54
55 Despite this excellent work, the Rankine (Rankine, 1882), Burgers-Rott (Burgers, 1948; Rott,
56 1958) and Sullivan (Sullivan, 1959) vortex model are still the most commonly used vortex models
57 to replicate tornado-like flow behaviour. An overview of some of the before mentioned vortex
58 models can be found in e.g. Kilty (2005), Batterson et al. (2007) and Kim and Matsui (2017).
59 However, with the increasing interest in the simulation of tornado-like flows, these models have
60 (in some cases and with varying degrees of success) been invoked in order to describe some
61 elements of the flow field. The authors feel that it is worth reflecting on the fundamental
62 assumptions behind these models and bench marking their performance against measured data
63 obtained in controlled conditions. For that reason, this paper gives detailed information about the
64 derivation and simplifications of the Rankine, Burgers-Rott and Sullivan vortex model. In addition
65 to the Rankine, Burgers-Rott and Sullivan vortex models, the recently published vortex model by
66 Baker and Sterling (2017), hereafter called 'Baker vortex model', is also included in the analysis.
67
68 Section two of this paper provides detailed information about the derivation and simplifications of
69 the above mentioned vortex models, while section three outlines the experimental methodology
70 used to assess the model suitability. The results of the model benchmarking can be found in section
71 four, with the main conclusions presented in section five.
72
73
74 **2. Existing vortex models**
75
76 *2.1 Flow field notation*
77
78 In what follows, a cylindrical coordinate system has been adopted as illustrated in figure 1. In
79 figure 1, r, z and θ are the radial distance, vertical distance and circumferential angle, respectively.

80 Thus, u_r, u_z and u_θ represent the radial, vertical and circumferential components of velocity. For
81 the sake of simplicity the flow is considered to be incompressible for all models and a density of
82 air of $\rho = 1.21\text{kg/m}^3$ is assumed for all calculations. In this section, a brief description of the
83 different vortex models examined in this paper is provided, together with the underlying
84 assumptions.
85
86 Using the aforementioned notation, the continuity equation (Eq. *1*) and radial (Eq. *2*),
87 circumferential (Eq. *3*) and vertical (Eq. *4*) components of the Navier-Stokes-Equations (NSE) can
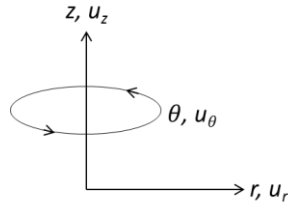88 be expressed as:

89
90   Figure 1: Flow field notation.
91
92

93
$$\frac{1}{r}\underbrace{\frac{\partial(ru_r)}{\partial r}}_{1} + \frac{1}{r}\underbrace{\frac{\partial u_\theta}{\partial \theta}}_{2} + \underbrace{\frac{\partial u_z}{\partial z}}_{3} = 0 \tag{1}$$

94

95
$$\underbrace{\frac{\partial u_r}{\partial t}}_{R1} + \underbrace{u_r\frac{\partial u_r}{\partial r}}_{R2} + \underbrace{\frac{u_\theta}{r}\frac{\partial u_r}{\partial \theta}}_{R3} - \underbrace{\frac{u_\theta^2}{r}}_{R4} + \underbrace{u_z\frac{\partial u_r}{\partial z}}_{R5} =$$

96
$$-\underbrace{\frac{1}{\rho}\frac{\partial p}{\partial r}}_{R6} + \underbrace{g_r}_{R7} + \nu\left(\underbrace{\frac{1}{r}\frac{\partial}{\partial r}\left(r\frac{\partial u_r}{\partial r}\right)}_{R8} - \underbrace{\frac{u_r}{r^2}}_{R9} + \underbrace{\frac{1}{r^2}\frac{\partial^2 u_r}{\partial \theta^2}}_{R10} - \underbrace{\frac{2}{r^2}\frac{\partial u_\theta}{\partial \theta}}_{R11} + \underbrace{\frac{\partial^2 u_r}{\partial z^2}}_{R12}\right) \tag{2}$$

97

98
$$\underbrace{\frac{\partial u_\theta}{\partial t}}_{C1} + \underbrace{u_r\frac{\partial u_\theta}{\partial r}}_{C2} + \underbrace{\frac{u_\theta}{r}\frac{\partial u_\theta}{\partial \theta}}_{C3} + \underbrace{\frac{u_r u_\theta}{r}}_{C4} + \underbrace{u_z\frac{\partial u_\theta}{\partial z}}_{C5} =$$

99
$$-\underbrace{\frac{1}{\rho r}\frac{\partial p}{\partial \theta}}_{C6} + \underbrace{g_\theta}_{C7} + \nu\left(\underbrace{\frac{1}{r}\frac{\partial}{\partial r}\left(r\frac{\partial u_\theta}{\partial r}\right)}_{C8} - \underbrace{\frac{u_\theta}{r^2}}_{C9} + \underbrace{\frac{1}{r^2}\frac{\partial^2 u_\theta}{\partial \theta^2}}_{C10} - \underbrace{\frac{2}{r^2}\frac{\partial u_r}{\partial \theta}}_{C11} + \underbrace{\frac{\partial^2 u_\theta}{\partial z^2}}_{C12}\right) \tag{3}$$

100

101
$$\underbrace{\frac{\partial u_z}{\partial t}}_{Z1} + \underbrace{u_r\frac{\partial u_z}{\partial r}}_{Z2} + \underbrace{\frac{u_\theta}{r}\frac{\partial u_z}{\partial \theta}}_{Z3} + \underbrace{u_z\frac{\partial u_z}{\partial z}}_{Z4} =$$

102
$$-\underbrace{\frac{1}{\rho}\frac{\partial p}{\partial z}}_{Z5} + \underbrace{g_z}_{Z6} + \nu\left(\underbrace{\frac{1}{r}\frac{\partial}{\partial r}\left(r\frac{\partial u_z}{\partial r}\right)}_{Z7} + \underbrace{\frac{1}{r^2}\frac{\partial^2 u_z}{\partial \theta^2}}_{Z8} + \underbrace{\frac{\partial^2 u_z}{\partial z^2}}_{Z9}\right) \tag{4}$$

103

104 Here ρ is the density of the fluid, t is the time, p is the static pressure and $\vec{g}$ is the gravity vector in
105 its different components. The different terms in equations $(1 - 4)$ have been labelled since, as will
106 be demonstrated below, it is possible to derive the majority of the analytical models by
107 disregarding different terms.

109 *2.2 Rankine vortex model*

111 The Rankine model has been adopted by a number of researchers (e.g. Hoecker, 1960; Church et
112 al., 1979; Winn et al., 1999; Wurman and Gill, 2000; Brown and Wood, 2004; Lee et al., 2004;
113 Mishra et al., 2008; Bech et al., 2009; Hashemi Tari et al., 2010; Wood and Brown, 2011; Refan
114 and Hangan, 2016; Tang et al., 2017) to model tornado-like flow behaviour. The following
115 assumptions are made in the derivation of the Rankine vortex model:

117 • *The flow field is one-dimensional and as such equations (2) and (4) can be disregarded.*
118 • *The flow field is steady state, i.e., term R1 can be taken as zero.*
119 • *The flow is inviscid ($\mu=0$), i.e., terms R8 - R12 can be neglected.*
120 • *Body forces can be neglected, i.e., ($\vec{g}=0$).*

122 These assumptions reduce the NSE to the cyclostrophic equation (Eq. *5*).

124
$$\frac{dp(r)}{dr} = \rho \, \frac{u_\theta(r)^2}{r} \qquad (5)$$

126 The Rankine model also assumes that the flow consists of two separate flow regions. In the first
127 region, the core region (i.e., $r < R$, where R is the core radius, which is defined as the radial distance
128 from the vortex centre at which the circumferential velocity component is maximal), the flow is
129 assumed to have a constant vorticity and is considered to be similar to that of a solid body. In the
130 second region, $(r > R)$ it is assumed that the flow can be described by a potential flow field
131 (incompressible, inviscid and irrotational) (Alekseenko et al., 2007) and is inversely proportional
132 to the radial distance. These assumptions enable the circumferential velocity component to be
133 modelled via an expression of the form:

135
$$\overline{u_\theta}(\bar{r}) = \begin{cases} \bar{r} & for \ (\bar{r} < 1) \\ \frac{1}{\bar{r}} & for \ (\bar{r} > 1) \end{cases} \qquad (6)$$

137 where $\overline{u_\theta}$ is the normalised circumferential velocity component $(= u_\theta/u_{\theta,max}$, where $u_{\theta,max}$ is
138 the maximum value of u_θ) and $\bar{r}$ is the radial distance normalised by the core radius, R. In equation
139 *6*, a discontinuity occurs at $\bar{r} = 1$. In order to avoid this, the model is occasionally modified as
140 shown in equation *6.1*. However, the most commonly used form is shown in equation *6* and hence
141 will be used in what follows.

142

$$\overline{u_\theta}(\bar{r}) = \frac{2\bar{r}}{(1+\bar{r}^2)} \tag{6.1}$$

144

145 Combining equation (6) with equation (5) and integrating, yields an expression for the normalised
146 pressure distribution of the Rankine vortex model (Eq. 7):

147

$$\bar{p}(\bar{r}) = \begin{cases} \overline{p_{(r=0)}} + \frac{1}{2}\left(\frac{r}{R}\right)^2 & for \ (\bar{r} < 1) \\ \overline{p_{r\to\infty}} - \frac{1}{2}\left(\frac{R}{r}\right)^2 & for \ (\bar{r} > 1) \end{cases} \tag{7}$$

149

150 where $\bar{p}(\bar{r})$ is the normalised pressure $(= p(r)/\rho u_{\theta,max}^2)$, $\overline{p_{r\to\infty}}$ is the normalised static
151 pressure, which is unaffected by the vortex and $\overline{p_{(r=0)}}$ is the static pressure at the vortex centre.

152

153 *2.3 Burgers-Rott vortex model*

154

155 The Burgers-Rott model has been adopted by a number of authors (e.g. Winn et al., 1999; Brown
156 and Wood, 2004; Lee et al., 2004, Kosiba and Wurman, 2010; Wood and Brown, 2011; Wurman
157 et al., 2013) to model tornado-like flow behaviour. Explicit in the derivation of the model are the
158 following assumptions:

159

- *The flow field is steady state, i.e., terms R1, C1 and Z1 are taken as zero.*
- *The viscosity is considered to be constant throughout the entire flow field.*
- *Body forces can be neglected, i.e., ($\vec{g}=0$).*
- *The circumferential velocity component is assumed to be solely dependent on the radial distance ($u_\theta = u_\theta(r)$).*
- *The vertical velocity component is assumed to be solely and linearly dependent on the vertical distance ($u_z = u_z(z)$ and $u_z \propto z$).*
- *As a result of the last two assumptions, the radial velocity component is solely and linearly dependent on the radial distance ($u_r = u_r(r)$ and $u_r \propto r$).*
- *The static pressure is assumed to be solely dependent on radial and vertical distances ($p = p(r,z)$).*

171

172 The above assumptions reduce equations (1 – 4) to the following simplified versions:

173

$$\frac{1}{r}\frac{\partial(ru_r)}{\partial r} + \frac{\partial u_z}{\partial z} = 0 \tag{1*}$$

175

$$u_r\frac{\partial u_r}{\partial r} - \frac{u_\theta^2}{r} = -\frac{1}{\rho}\frac{\partial p}{\partial r} + \nu\left(\frac{1}{r}\frac{\partial}{\partial r}\left(r\frac{\partial u_r}{\partial r}\right) - \frac{u_r}{r^2}\right) \tag{2*}$$

177

5

$$u_r \frac{\partial u_\theta}{\partial r} + \frac{u_r u_\theta}{r} = \nu \left(\frac{1}{r} \frac{\partial}{\partial r} \left(r \frac{\partial u_\theta}{\partial r} \right) - \frac{u_\theta}{r^2} \right) \tag{3*}$$

178

179

$$u_z \frac{\partial u_z}{\partial z} = -\frac{1}{\rho} \frac{\partial p}{\partial z} \tag{4*}$$

180

181

182 Now, the Burgers-Rott model acknowledges that the flow within a tornado-like structure is likely
183 to be subject to changing levels of vorticity, which in turn will have implications for the associated
184 pressure field. Thus, it is assumed that the vertical velocity component changes with respect to
185 height and the following relationship is adopted:

186

187
$$\overline{u_z}(\bar{z}) = 2\bar{a}\bar{z} \tag{8}$$

188

189 where $\overline{u_z}(\bar{z})$ is the normalised vertical velocity ($= u_z(z)/u_{\theta,max}$), $\bar{z}$ is the normalised vertical
190 height ($= z/R$) and $\bar{a}$ is a constant, whose magnitude purports to account for the strength of vortex
191 stretching. It is also assumed that $\bar{a}$ is related to the viscous dissipation, ν, via an expression of the
192 form:

193
$$\bar{a} = \frac{2\nu}{Ru_{\theta,max}} \tag{8.1}$$

194

195 Equation (8.1) implies that the viscous dissipation, ν, continuously removes kinetic energy from
196 the flow, which is continuously introduced by vortex stretching. Using equation (8) and integrating
197 the simplified continuity equation (Eq. 1*), an expression for the normalised radial velocity
198 component, $\overline{u_r}$, can be obtained (Eq. 9).

199

200
$$\overline{u_r}(\bar{r}) = -\bar{a}\bar{r} \tag{9}$$

201

202 Using equations (8) and (9), and solving the simplified NSE in the circumferential direction (Eq.
203 3*), an expression for the normalised circumferential velocity component, $\overline{u_\theta}$, can be found (Eq.
204 10).

205

206
$$\overline{u_\theta}(\bar{r}) = \frac{1}{\bar{r}} \left(1 - exp(-\bar{r}^2) \right) \tag{10}$$

207

208 It is perhaps worth noting that $\overline{u_z}$ and $\overline{u_r}$ increase to infinity as $\bar{z} \rightarrow \infty$ and $\bar{r} \rightarrow \infty$, respectively,
209 which, it is suggested, may not be representative of a tornado-like flow structure.

210

211 The pressure distribution of the Burgers-Rott vortex model can be obtained by solving the
212 simplified NSE (Eq. 2* and Eq. 4*) using the model velocities (Eq. 8, Eq. 9, and Eq. 10). This
213 leads to the following equation for the normalised pressure distribution (Eq. 11).

214

215
$$\overline{p_{Burgers}}(\bar{r}, \bar{z}) = \bar{p}(0,0) + \int_0^{\bar{r}} \frac{\overline{u_\theta}(\bar{r}\prime)^2}{\bar{r}\prime} d\bar{r}\prime - \frac{\bar{a}^2}{2} (\bar{r}^2 + 4\bar{z}^2) \tag{11}$$

216
217 *2.4 Sullivan vortex model*
218
219 The Sullivan model has also been adopted by a few researchers (e.g. Winn et al., 1999; Wood and
220 Brown, 2011) to model tornado-like flow behaviour. The assumptions for this vortex model are:
221

222 • *The flow field is steady state, i.e., terms R1, C1 and Z1 are taken as zero.*
223 • *The viscosity is considered to be constant throughout the entire flow field.*
224 • *Body forces can be neglected, i.e., ($\vec{g}$=0).*
225 • *The circumferential velocity component is assumed to be solely dependent on the radial*
226 *distance ($u_\theta = u_\theta(r)$).*
227 • *The vertical velocity component is assumed to be only dependent on radial and vertical*
228 *distances. The dependence on the vertical distance is linear ($u_z = u_z(r,z)$ and $u_z \propto z$).*
229 • *As a result of the last two assumptions, the radial velocity component is solely dependent*
230 *on the radial distance ($u_r = u_r(r)$).*
231 • *The static pressure is assumed to be solely dependent on radial and vertical distances ($p =$*
232 *$p(r,z)$).*
233

234 The above assumptions reduce the continuity equation (*1*), radial and circumferential components
235 of the NSE (*2 – 3*) to simplified versions shown in equations (*1* – 3**). For the vertical component
236 of the NSE (*4*) the following simplified versions is obtained.
237

$$u_z \frac{\partial u_z}{\partial z} + u_z \frac{\partial u_z}{\partial z} = -\frac{1}{\rho} \frac{\partial p}{\partial z} + \nu \left(\frac{1}{r} \frac{\partial}{\partial r} \left(r \frac{\partial u_z}{\partial r} \right) \right) \qquad (4^{**})$$

239

240 One main difference of the Sullivan model compared to the Burgers-Rott model lies in the
241 complexity of the model solution. While the Burgers-Rott vortex model only allows single-celled
242 vortices to be generated, the Sullivan model potentially enables solutions for single and two-celled
243 vortices to be obtained; this is obtained via the use of a shape parameter, *b* (Eq. *12* and Eq. *13*).
244 The effect of this parameter on the tornado-like flow field will be discussed in detail in section 2.7.
245 Unless stated otherwise, *b* = 3. The required vortex stretching is generated by suction at relatively
246 large heights and is achieved by a non-linear increase of the vertical velocity component with
247 height, as illustrated in equation (*12*). The same normalisation used for the Burgers-Rott vortex
248 model is applied for the Sullivan vortex model.
249

$$\overline{u_z}(\bar{r}, \bar{z}) = 2\bar{a}\bar{z}\big(1 - b \cdot exp(-\bar{r}^2)\big) \qquad (12)$$

251

252 Following the procedure described for the Burgers-Rott vortex model, expressions for $\overline{u_r}$ (Eq. *13*)
253 and $\overline{u_\theta}$ (Eq. *14*) can be obtained.
254

$$\overline{u_r}(\bar{r}) = -\bar{a}\bar{r} + \frac{2b\bar{v}}{\bar{r}}\left(1 - exp(-\bar{r}^2)\right) \tag{13}$$

$$\overline{u_\theta}(\bar{r}) = \frac{1}{\bar{r}}\frac{H(x)}{H(\infty)} \tag{14}$$

with $x = \bar{r}^2$ and $H(x) = \int_0^x exp\left(-x' + 3\int_0^{x'}\frac{1}{x''}(1 - exp(-x''))dx''\right)dx'$

It is perhaps worth noting, that for $\bar{r} = 0$ and $\bar{z} \to \infty$ the magnitude of $\overline{u_z}$ increases to infinity. Furthermore, also $\overline{u_r}$ increases to infinity for $\bar{r} \to \infty$ (Eq. *13*). Similar to the Burgers-Rott model, it is suggested that this behaviour may be physically unrealistic in a tornado-like structure.

The pressure distribution of the Sullivan vortex model can be obtained by solving the simplified NSE (Eq. *2** and *4**) using the model velocities (Eq. *12 - 14*). This leads to the following equation for the normalised pressure distribution:

$$\overline{p_{Sullivan}}(\bar{r},\bar{z}) = \overline{p_{Burgers}}(\bar{r},\bar{z}) - \frac{18\bar{v}^2}{\bar{r}^2}\left(1 - exp(-\bar{r}^2)\right)^2 \tag{15}$$

2.5 Baker vortex model

Baker and Sterling (2017) developed a vortex model, which can reproduce the flow and pressure characteristics of a single and two-celled vortex. In order to enable comparisons with the aforementioned models, only the solution for the single-cell vortex with radial inflow and vertical updraft is analysed in this paper. The following assumptions are made in the derivation of the Baker vortex model:

- *The flow field is steady state, i.e., terms R1, C1 and Z1 are taken as zero.*
- *The flow is inviscid, i.e., terms R8 - R12, C8 - C12 and Z7 - Z9 can be disregarded.*
- *Body forces can be neglected, i.e., ($\vec{g}$=0).*
- *The circumferential velocity component is assumed to be dependent on radial and vertical distance ($u_\theta = u_\theta(r, z)$).*
- *The radial velocity component is assumed to be only dependent on radial and vertical distances ($u_r = u_r(r, z)$).*
- *As a result of the last two assumptions, the vertical velocity component is solely dependent on radial and vertical distances ($u_r = u_r(r, z)$).*
- *The static pressure is assumed to be solely dependent on radial and vertical distances ($p = p(r, z)$).*

These assumptions reduce the continuity equation (*1*) to the simplified version shown in equation (*1**) and the NSE (Eq. *2 - 4*) to the following simplified versions:

293
$$u_r \frac{\partial u_r}{\partial r} - \frac{u_\theta^2}{r} + u_z \frac{\partial u_r}{\partial z} = -\frac{1}{\rho} \frac{\partial p}{\partial r} \qquad (2{***})$$

294

295
$$u_r \frac{\partial u_\theta}{\partial r} + \frac{u_r u_\theta}{r} + u_z \frac{\partial u_\theta}{\partial z} = 0 \qquad (3{***})$$

296

297
$$u_r \frac{\partial u_z}{\partial r} + u_z \frac{\partial u_z}{\partial z} = -\frac{1}{\rho} \frac{\partial p}{\partial z} \qquad (4{***})$$

298

299   In addition, the Baker model assumes that the radial velocity component takes the following form:

300

301
$$\overline{u_r}(\bar{r}, \bar{z}) = \frac{-4\bar{r}\bar{z}}{(1+\bar{r}^2)(1+\bar{z}^2)} \qquad (16)$$

302

303   One of the potential advantages of this model compared to the Rankine, Burgers-Rott and Sullivan
304   vortex models is that the radial velocity component is assumed to show a more realistic behaviour
305   (Eq. *16*), i.e., rather than increasing to infinity for large radial distances, a maximum value is
306   reached at $r = r_m$ which then falls to zero for $r = 0$ and $r = \infty$. In the vertical direction, the radial
307   velocity distribution shows an attempt to replicate the tornado boundary layer by assuming a
308   maximum in the radial velocity component at a known distance above the ground $(z = z_m)$. For z
309    $= 0$ and $z = \infty$ the radial velocity falls to zero. Since the Baker vortex model focuses on the
310   distribution of the radial velocity component, different parameters are chosen for the normalisation
311   of velocities, radial and vertical distances. Velocities are normalised by the maximum radial
312   velocity $(u_r(r_m, z_m) = u_{r,max})$ and radial and vertical distances are normalised by r_m and z_m,
313   respectively.

314

315   Using equation (*16*) and integrating the simplified continuity equation (*1**), an expression for the
316   normalised vertical velocity component, $\overline{u_z}$, can be obtained as follows:

317

318
$$\overline{u_z}(\bar{r}, \bar{z}) = \frac{4\delta \, ln(1+\bar{z}^2)}{(1+\bar{r}^2)^2} \qquad (17)$$

319

320   where δ is the ratio z_m / r_m. Using equations (*16*) and (*17*), and solving the simplified NSE in the
321   circumferential direction (Eq. *3****), the following expression for the normalised circumferential
322   velocity component, $\overline{u_\theta}$, can be obtained:

323

324
$$\overline{u_\theta}(\bar{r}, \bar{z}) = \frac{K\bar{r}^{\gamma-1}\left[ln(1+\bar{z}^2)\right]^{\gamma/2}}{(1+\bar{r}^2)^{\gamma/2}} \qquad (18)$$

325

326   Here, γ is a shape parameter (an arbitrary real number which can be used to adjust the shape of the
327   circumferential velocity profile). K is a constant and related to Baker's definition of the swirl ratio,
328   i.e., $S_{Baker} = 0.347\,K$. The swirl ratio in the Baker vortex model is defined as the ratio of $u_\theta(r_m, z_m)$
329   and $u_r(r_m, z_m)$. It is perhaps worth noting that $\overline{u_\theta}$ increases to infinity for $z \to \infty$. This increase is

9

330 assumed to be realistic for the lowest heights, relatively close to the surface, where surface
331 roughness affects the vertical velocity distribution but becomes physically unrealistic for larger
332 heights.

333

334 The pressure distribution of the Baker vortex model can be obtained by solving the simplified NSE
335 (Eq. *2**** and Eq. *4****) using the model velocities (Eq. *16 – 18*) and, assuming a shape parameter
336 of $\gamma = 2$:

337

338
$$\overline{p_{Baker}}(\bar{r},\bar{z}) = -\frac{8\bar{r}^2\bar{z}}{(1+\bar{r}^2)^2(1+\bar{z}^2)^2} - \frac{4.15 S_{Baker}^2\left(ln(1+\bar{z}^2)\right)^2}{(1+\bar{r}^2)} - \frac{4ln(1+\bar{z}^2)(1-\bar{z}^2)}{(1+\bar{r}^2)^2(1+\bar{z}^2)^2} \qquad (19)$$

339

340 It is worth noting that the surface pressure distribution equals zero for $z = 0$. This behaviour is
341 physically unrealistic in a tornado-like structure and is discussed in Baker and Sterling (2017). It
342 is assumed that pressure variations in the vertical direction can be neglected within the boundary
343 layer ($z < z_m$) (Baker and Sterling, 2017) and consequently, it is assumed that $\overline{p_{Baker}}(\bar{r},\bar{z} < 1) =$
344 $\overline{p_{Baker}}(\bar{r},\bar{z} = 1)$.

345

346 *2.6 Circumferential velocity component*

347

348 Unlike the Rankine, Burgers-Rott and Sullivan vortex models, the Baker model has a shape
349 parameter, γ, which enables the shape of the circumferential velocity profile to be varied. The
350 effect of this parameter on the circumferential velocity field is illustrated in table 1 and figure 2. It
351 is perhaps worth noting that γ is related to $\bar{r}$ in the following way ($\bar{r}^2 = \gamma - 1$) (Baker and
352 Sterling, 2017). Consequently, for $\gamma \leq 1$, the circumferential velocity component becomes
353 physically unreasonable. Thus, to ensure results, which describe the behaviour of a forced vortex
354 at the centre, and a free vortex at larger radial distances, Baker and Sterling (2017) recommend
355 setting $\gamma = 2$.

356

357 Table 1 illustrates the ratio of $u_{\theta,max}$ and R of the corresponding models compared to the Rankine
358 vortex model with input parameters of $R = 10$m and $u_{\theta,max} = 10$m/s. For the Baker vortex model
359 a swirl ratio of $S_{Baker} = 1$ is assumed and readings for the maximum circumferential velocity
360 component are taken at $z = z_m$. Table 1 shows that Burgers-Rott and Sullivan vortex models
361 underestimate the actual input velocity by a factor of *0.64* and *0.32,* respectively, and overestimate
362 the core radius position, R, by a factor of *1.12* and *2.29* respectively. For the Baker vortex model
363 with a shape parameter of $\gamma = 2$, the radius at which $\overline{u_r}$ attains a maximum, is identical to the core
364 radius of the Baker vortex model and is also identical to the actual input core radius ($r_m = R_{Baker} =$
365 R). Hence, the Rankine and Baker model results for $\gamma = 2$ in table 1 are identical. With increasing γ,
366 R_{Baker} increases and the magnitude of $u_{\theta,max,Baker}$ decreases (Table 1). For $\gamma = 3$, R and $u_{\theta,max}$ of
367 Baker and Burgers-Rott vortex model are similar and show a decrease in $u_{\theta,max}$ by about
368 $1/3 \times u_{\theta,max,Rankine}$ (Table 1). For $\gamma = 5$, R and $u_{\theta,max}$ of Baker and Sullivan vortex model are

369 similar and show a core radius, which is about $2 \times R_{Rankine}$ and a decrease in $u_{\theta,max}$ by about $2/3 \times$

370 $u_{\theta,max,Rankine}$ (Table 1). Thus, in what follows, care has been taken to normalise, by the relevant

371 model values of each vortex model as opposed to a standard value.

372

373 Table 1: Ratios of $u_{\theta,max}$ and R of the corresponding vortex models compared to the Rankine vortex model.

374

	$\dfrac{u_{\theta,max,x}}{u_{\theta,max,Rankine}}$	$\dfrac{R_x}{R_{Rankine}}$
x=Rankine	1	1
x=Burgers	0.64	1.12
x=Sullivan	0.32	2.29
x=Baker (γ=2, z=z_m)	1	1
x=Baker (γ=3, z=z_m)	0.64	1.41
x=Baker (γ=5, z=z_m)	0.33	2.0

386

387 Figure 2 shows that among the four vortex models, large differences in the circumferential velocity

388 are found for $r < R_{model}$ between Sullivan and Baker vortex model with a shape parameter of $\gamma =$

389 2 (Figure 2). This is not surprising as these vortex models represent two entirely different tornado

390 flow types. The Sullivan model represents a two-celled vortex whereas the Baker model shows a

391 single-celled vortex structure. A single-celled vortex is defined as a relatively narrow column of

392 rising and rotating air. With increasing rotational energy, a downdraft forms in the vortex centre

393 and terminates aloft a stagnation point above which the vortex increases significantly in size

394 (Trapp, 2000). This vortex transformation is known as 'vortex breakdown'. With a further increase

395 in rotational energy, the stagnation point lowers towards the ground. In a two-celled vortex, the

396 downdraft reaches the ground and therefore decreases $\overline{u_\theta}$ close to $r = 0$ whereas the structure of

397 the single-celled vortex shows a strong non-linear increase of $\overline{u_\theta}$ inside the vortex core ($r < R_{model}$)
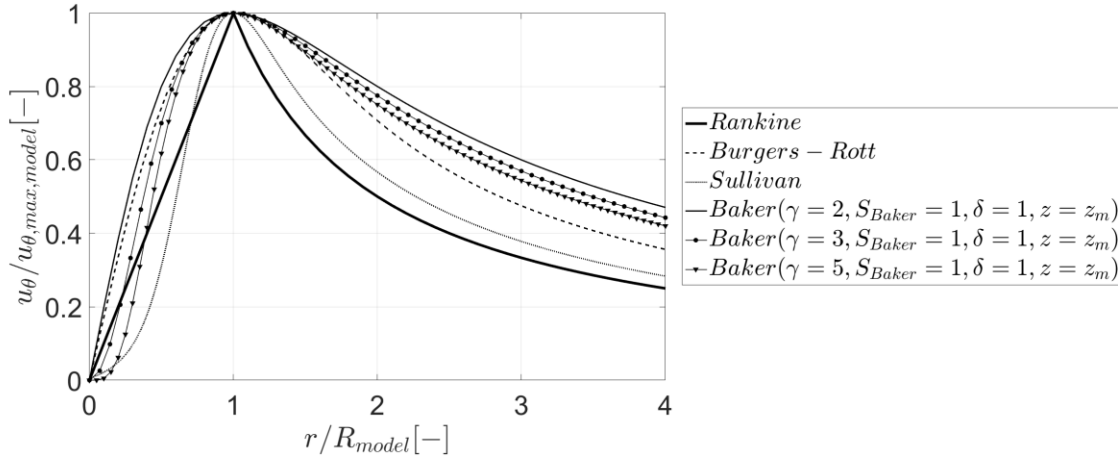
398 (Figure 2).

399

Figure 2: Circumferential velocity component of the Rankine, Burgers-Rott, Sullivan and Baker vortex model.

For the Baker model, close to the vortex core, $\overline{u_\theta}$ increases at a slower rate with increasing γ, and the circumferential velocity profile tends towards the shape of a two-celled vortex structure (Figure 2) (compared to the Sullivan vortex model). For larger radial distances ($r > R_{model}$), $\overline{u_\theta}$ of the Baker vortex model decreases at a slower rate compared to the other three models and largest differences are found between Rankine and Baker vortex model ($\gamma = 2$). Differences in the circumferential velocity of all vortex models decrease as $r \to \infty$.

The effect of γ on the circumferential velocity component with height is shown in Figure 3. For relatively small vertical distances from the surface, $\overline{u_\theta}$ increases at a slower rate the larger γ is. With increasing vertical distance, this behaviour reverses and $\overline{u_\theta}$ increases faster with height as γ increases (Figure 3). Furthermore, figure 3 shows that independent from γ, $\overline{u_\theta}$ increases to infinity for $z \to \infty$, albeit at different rates. It needs to be mentioned that the Baker vortex model is the only model that takes a height dependence of u_θ into account. However, it does not represent the vertical profile of the circumferential velocity observed in simulated tornado-like vortices or full-scale. For instance, Tang et al. (2017) showed that u_θ increases rapidly in the lowest heights with the maximum circumferential velocity relatively close to the ground. With further increasing height $\overline{u_\theta}$ decreases and remains relatively uniform in even greater heights. Refan et al. (2017) showed that a similar behaviour was observed in five different full-scale tornadoes of different intensity and flow structure.

12

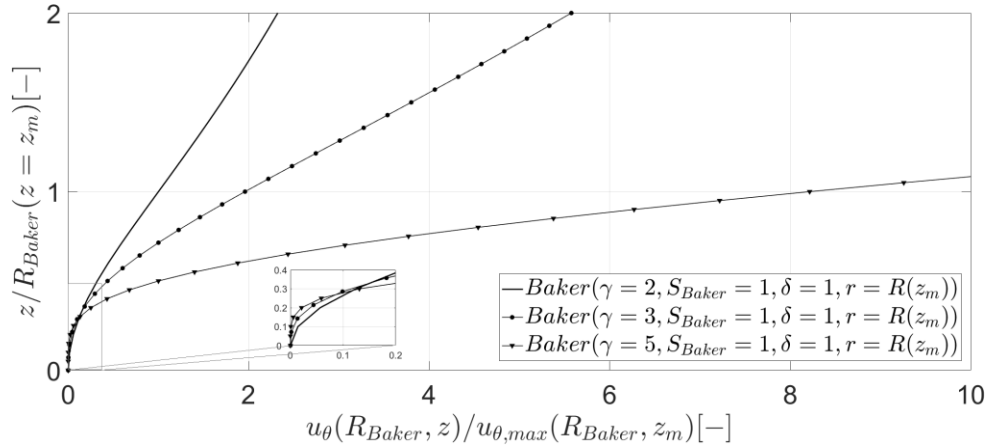Figure 3: Circumferential velocity component of the Baker vortex model in different heights for different γ values.

Another parameter that influences the shape of the circumferential velocity profile is the swirl ratio, S_{Baker}. The magnitude of u_θ increases as the value of S_{Baker} increases. The position of the core radius and the shape of the circumferential velocity profile are independent from the chosen swirl ratio. For that reason, the effect of S_{Baker} on u_θ cannot be seen when normalising u_θ with $u_{\theta,max,Baker}$ and radial distances with R_{Baker}.

*2.7 Radial and vertical velocities and shape parameters*

The Baker model is not the only model to employ a shape component. As shown in equation (*8*) and (*12*), both, the Burgers-Rott and Sullivan model also include a 'constant' to 'correct' the vertical velocity. In addition, both models have a 'viscosity' parameter explicitly included in the circumferential velocity component (which is not evident in equations (*10*) and (*14*) due to the normalisation adopted and assuming the relationship given in equation (*8.1*)). If it is assumed that the viscosity parameter corresponds to the kinematic viscosity of air (i.e., $v \sim 10^{-5}$ m^{2}s^{-1} at 20 °C), then the calculated radial and vertical velocity components of the Burgers-Rott and Sullivan vortex models are small. Hence, to ensure reasonable magnitudes of the velocity components (Figures 4 and 5), the viscosity needs to be increased by several orders of magnitude (Davies-Jones and Kessler, 1974). Thus, in this context, the 'viscosity' parameter is essentially nothing more than a 'simple' shape parameter.

Figures 4 and 5 show the effect of the 'viscosity' parameter on the radial and vertical velocity distributions of the Burgers-Rott and Sullivan vortex models. For the Burgers-Rott vortex model, a larger 'viscosity' parameter results in larger vertical and radial velocities (Figure 4). Hence, the larger the value of v becomes, the greater the radial inflow towards the vortex centre and the stronger the vertical updraft gets (Figure 4). For the Sullivan vortex model, an increase in v results in larger negative vertical velocities for $r < R_{Sullivan}$, and larger positive vertical velocities for $r > R_{Sullivan}$ (Figure 5). For the radial velocity, the larger v is, the stronger the radial outflow at $r <$

13

453 $R_{Sullivan}$, and the stronger the radial inflow for $r < R_{Sullivan}$ gets (Figure 5). The radial distance at
454 which radial and vertical velocity components change sign is not affected by changes in the
455 'viscosity' parameter (Figure 5). This means that the size of the downdraft region close to $r = 0$ is
456 independent of ν.
457
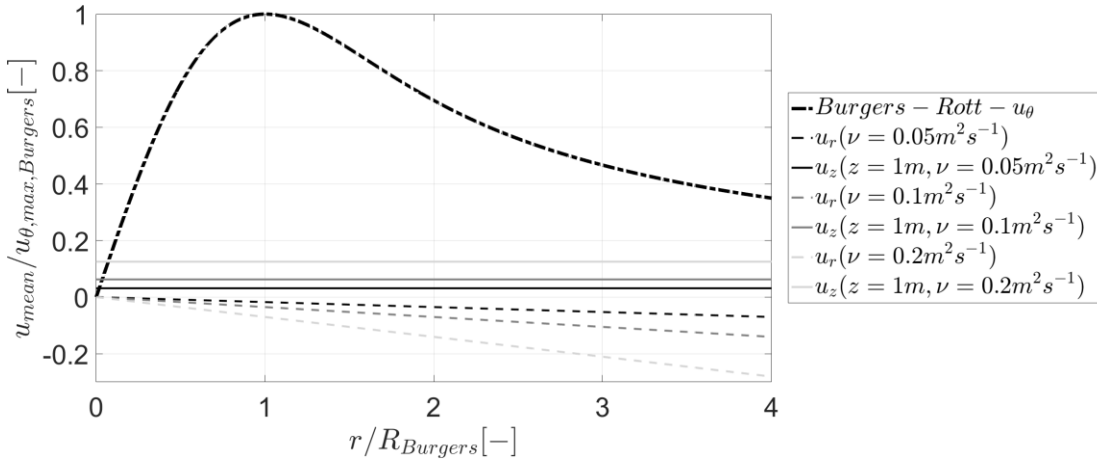
458

459 Figure 4: Velocity components of the Burgers-Rott vortex model for different 'viscosity' values.
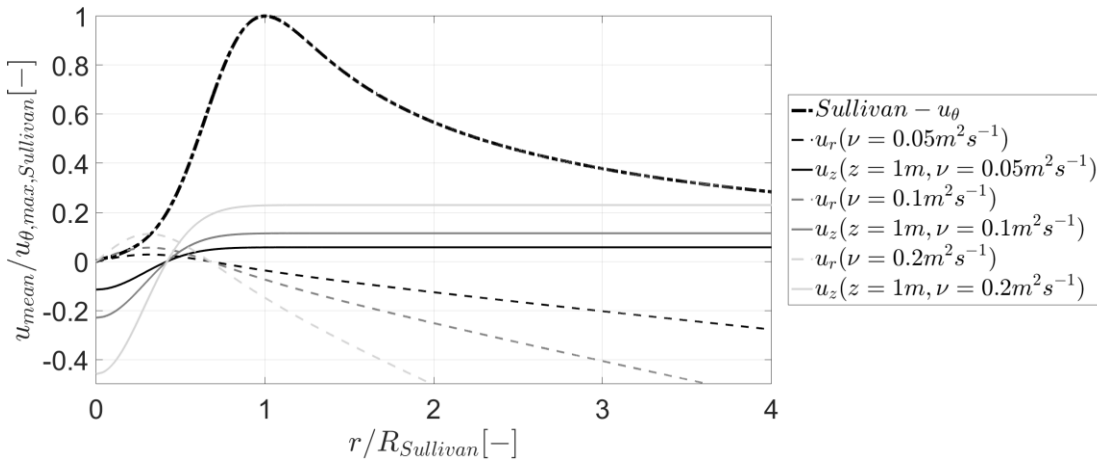
460

461 Figure 5: Velocity components of the Sullivan vortex model for different 'viscosity' values.
462

463 An additional shape parameter contained in the Sullivan vortex model is denoted as b, which
464 influences the distribution of radial and vertical velocity components and can be adjusted to model
465 solutions for single and two-celled vortices. Figure 6 illustrates the effect of b on the radial and
466 vertical flow field of the Sullivan vortex model. For $b = 0$, radial and vertical velocity components
467 of the Sullivan vortex model are identical to the solutions obtained from the Burgers-Rott vortex
468 model. For $b > 1$, a two-celled structure can be obtained, which is indicated by negative vertical
469 velocities close to the vortex centre. The greater the magnitude of b gets, the more negative the
470 vertical velocities in the vortex centre become, and additionally, the further the downdraft region
471 extends in the radial direction. For $r > R_{Sullivan}$, the vertical velocity converges to a value, which is
472 independent of b but dependent on the height. Radial outflow velocities inside the vortex core are

14

473 larger for larger *b* values, and the larger *b* gets, the larger the region of radial outflow extends
474 radially (Figure 6). Radial inflow velocities obtained with a lower *b* value increase slightly faster
475 in magnitude close to the vortex core but converge for larger radial distances (Figure 6). Hence,
476 differences of *b* are only significant inside the vortex core.
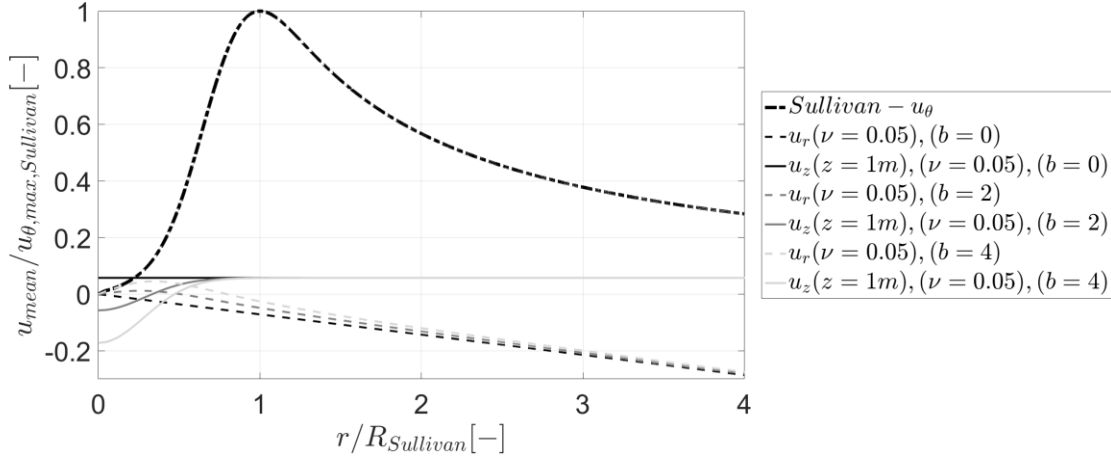

477
478 Figure 6: Velocity components of the Sullivan model for different *b* values.
479

480 The vertical velocity component of the Baker vortex model depends on the value of δ. The vertical
481 velocity component at the vortex centre increases with increasing δ (Figure 7a). Additionally,
482 figure 7b shows that the vertical velocity component increases faster with height as δ increases.

483 a)

b)
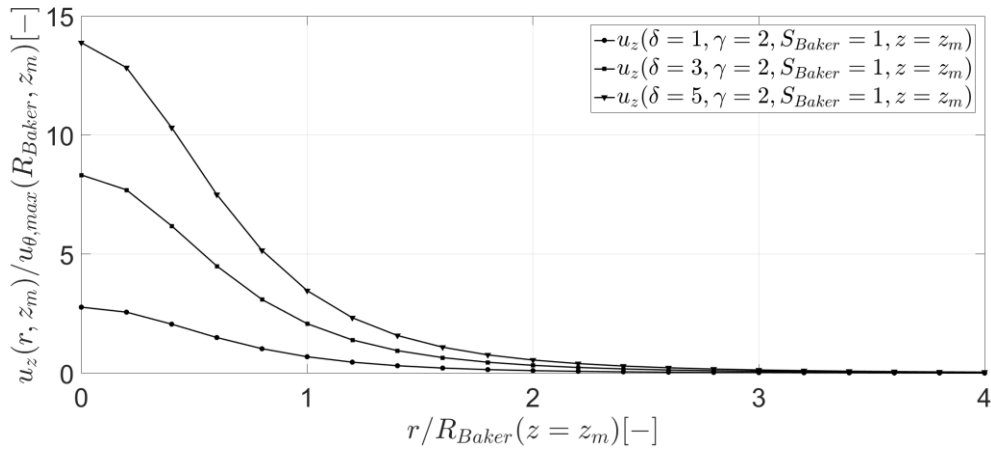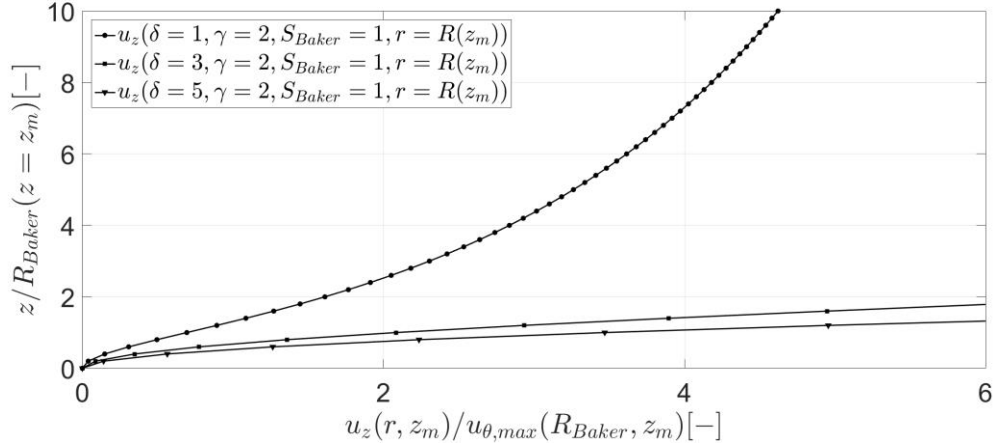
Figure 7: The effect of δ on the vertical velocity component of the Baker vortex model for different radial distances (a) and heights (b).

2.8 The static surface pressure distribution

The surface pressure distribution of Rankine, Burgers-Rott and Sullivan vortex models are shown in figure 8 for the case of $v = 0$. This restriction implies that the surface pressure distributions of the Burgers-Rott and Sullivan vortex models are solely dependent on the circumferential velocity profile of the corresponding vortex model and equations (*11*) and (*15*) simplify to:

$$\overline{p_{Burgers}}(\bar{r}, \bar{z}) = \overline{p_{Sullivan}}(\bar{r}, \bar{z}) = \bar{p}(0,0) + \int_0^{\bar{r}} \frac{\overline{u_\theta}(\bar{r}')^2}{\bar{r}'} d\bar{r}'. \tag{20}$$

The last term on the right hand side gives the largest contribution to the entire pressure distribution of the Burgers-Rott and Sullivan vortex model. Thus, its value defines the magnitude of surface pressure increase from the vortex centre towards larger radial distances and is determined by the area under the circumferential velocity profile shown in figure 2. For that reason, this term is largest for the Burgers-Rott vortex model and results in what maybe a physically unrealistic surface pressure increase from the vortex centre (Figure 8). For the Sullivan vortex model, the magnitude of this term is of the same order as that one of the Rankine vortex model.

The entire pressure distribution of the Burgers-Rott and Sullivan vortex models, depend on the contribution of the circumferential, radial and vertical velocity (Eq. *11* and Eq. *15*), and therefore is dependent on the 'viscosity' parameter. Also shown in Figure 8, is the effect of v on the pressure distribution. The decrease in surface pressure with increasing radial distance originates from a combination of the vertical updraft and the potentially unrealistic increase in radial velocity, i.e., $\frac{\bar{a}^2}{2}(\bar{r}^2 + 4\bar{z}^2)$. These terms are identical in Burgers-Rott and Sullivan vortex models, however, the different trends shown in figure 8 arise due to the normalisation, since $R_{Sullivan} > R_{Burgers\text{-}Rott}$.

16

513 The additional term in the surface pressure distribution of the Sullivan vortex model (i.e.,

514 $-\frac{18\bar{v}^2}{\bar{r}^2}\left(1 - exp(-\bar{r}^2)\right)^2$) describes the effect of the non-linear behaviour of radial and vertical

515 velocity components inside the vortex core on the pressure distribution. The downdraft close to

516 the centre of the vortex increases the surface pressure distribution and places the minimum pressure

517 at the radial position where vertical and radial velocity components are zero (Figure 8).
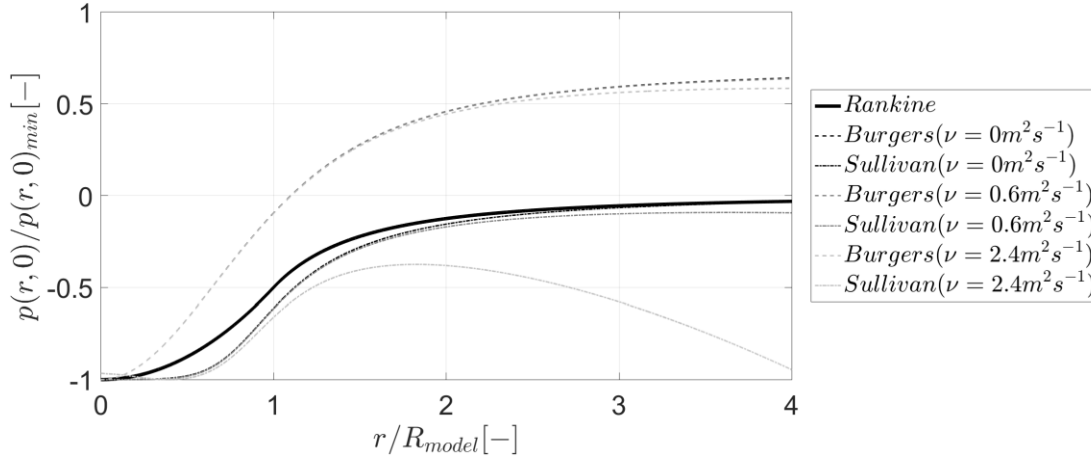
518
519 Figure 8: Surface pressure distribution of Rankine, Burgers-Rott and Sullivan vortex model for different 'viscosity'
520 values.
521

522 In order to enable a meaningful comparison of the surface pressure distributions, the 'viscosity'
523 parameter, v, and the 'vortex stretching' parameters $\bar{a}$, need to be adjusted in the circumferential
524 velocity and surface pressure distribution of the Burgers-Rott vortex model. This ensures that the
525 increase in surface pressure is of similar order to that one of the Rankine and Sullivan vortex
526 model. Thus, equation (*10*) needs to be modified by means of the relation given in equation (*8.1*)
527 in the following way (Eq. *21*) to obtain a circumferential velocity distribution for the Burgers-Rott
528 vortex model, which is dependent on v and $\bar{a}$ (Eq. *21*).
529

530
$$\overline{u_\theta}(\bar{r}) = \frac{1}{\bar{r}}\left(1 - exp\left(-\frac{r\bar{a}\,u_{\theta,max}}{2v}\right)^2\right) \tag{21}$$

531

532 v and $\bar{a}$ need to be chosen independent from one another, which has the consequence that the input
533 parameters, R and $u_{\theta,max}$ vary (see Eq. *8.1*). Unquestionably, this is physically not consistent but
534 seems to be the only way for the Burgers-Rott vortex model to generate a physically meaningful
535 surface pressure increase with increasing radial distance.
536

537 Figure 9 shows the surface pressure distribution for input parameters of $R = 10$m and $u_{\theta,max} = $
538 10m/s for the Rankine, Burgers-Rott and Sullivan models. It is worth noting that the 'viscosity'
539 and 'stretching' parameter differ for different input parameters. The two-celled structure of the
540 Sullivan vortex, and hence, the decreased circumferential velocity component close to the vortex
541 core result in a relatively flat pressure distribution close to the vortex centre (Figure 8). The surface

542 pressure distribution of the Burgers-Rott vortex increases at a faster rate close to the vortex centre
543 due to a rapid increase in circumferential velocity in this region (Figure 8). The largest differences
544 in the surface pressure distribution of the vortex models can be found inside the vortex core ($r <$
545 R_{model}) and for radial distances around $r / R_{model} = 1.5$. This arises due to the relative differences in
546 the magnitude of the circumferential velocity predicted by the analytical models (section 2.6).
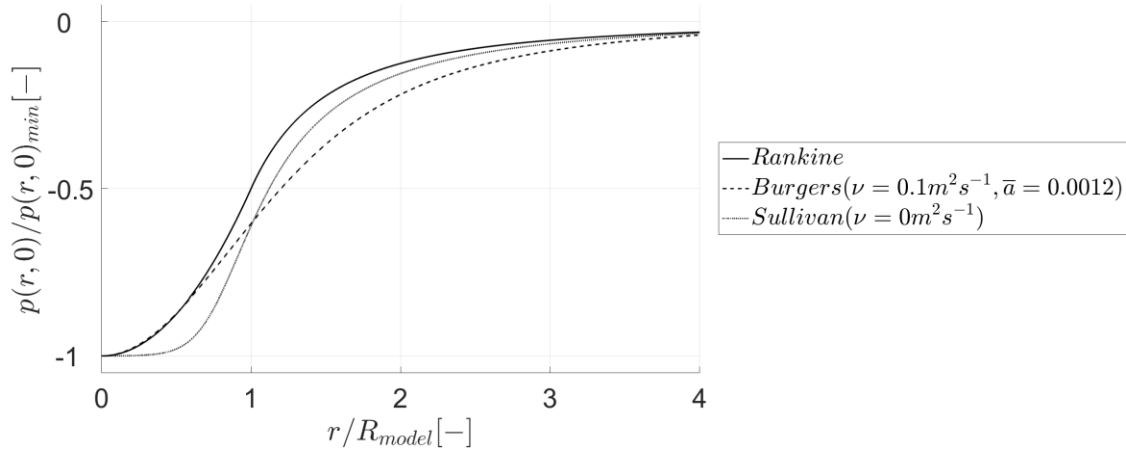
547
548 Figure 9: Surface pressure distribution of Rankine, adjusted Burgers-Rott and Sullivan vortex model.
549
550 The static 'surface pressure' distribution and the effect of the swirl ratio on the shape of the
551 distribution of the Baker vortex model is shown in figure 10. The 'surface pressure' distribution
552 of the Baker vortex model falls to zero for $r \to \infty$, however, the 'surface pressure' minimum is not
553 bounded for the Baker vortex model and decreases with increasing swirl ratio as shown in figure
554 10 from -1.99 $\times \rho u_r(r_m, z_m)$ to -17.94 $\times \rho u_r(r_m, z_m)$ for $S_{Baker} = 1$ to 3 due to the term
555 $-\dfrac{4.15 S_{Baker}{}^2 \left(ln\left(1+\bar{z}^2\right)\right)^2}{(1+\bar{r}^2)}$ (compare equation (*19*)). The effect of this on the 'surface pressure'
556 distribution is masked in figure 10 due to normalising the pressure distribution additionally with
557 $p(r, z_m)_{min}$ of the corresponding swirl ratio. This additional normalisation is applied to force all
558 pressures to tend to -1 as *r/R* tends to 0. It is noted that some numerical and experimental data,
559 e.g., Natarajan and Hangan (2012) and Haan et al. (2008), show that the surface pressure minimum
560 decreases in magnitude with increasing swirl ratio which has been associated with a transition from
561 a single-celled to a two-celled vortex. At present, although the Baker model is able to represent
562 multiple cell tornadoes, this behaviour is not incorporated into the current paper.
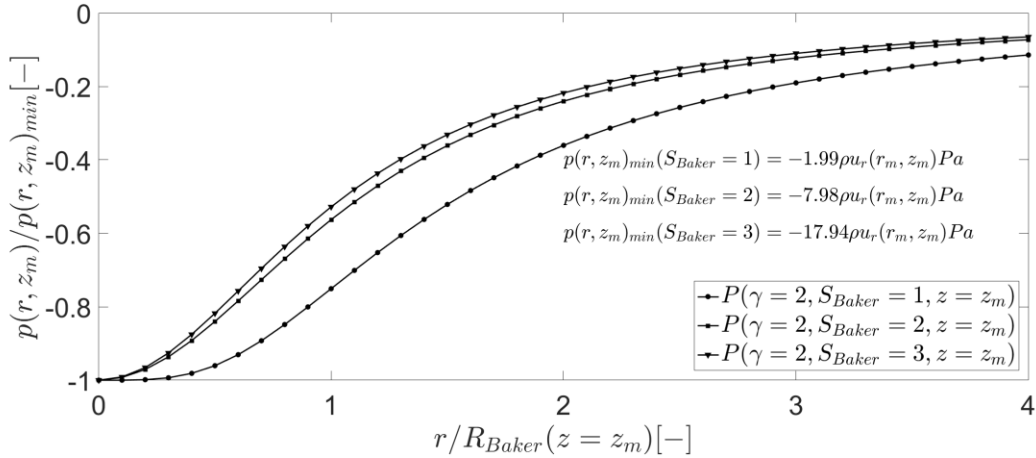563

The effect of the radial velocity profile on the 'surface pressure' is, not surprisingly, largest at the core radius (R_{Baker}) since this is where the radial velocity is maximum for $\gamma = 2$. When this term is normalised by the value of $p(r,z_m)_{min}$ for each corresponding swirl ratio, its magnitude changes and results in a different distribution of relative pressure (Figure 10). As a consequence, figure 10 shows that with increasing S_{Baker} the rate of change of pressure with increasing radial distance increases and hence, the smaller the vortex becomes. It needs to be mentioned here that this is only the case because the core radius (R_{Baker}) remains constant even though the swirl ratio changes. Due to the shape of the radial velocity component, differences in figure 10 are largest at $r / R_{Baker} (z = z_m) = 1$. The last term in equation (*19*) represents the effect of vertical advection of radial velocity on the 'surface pressure' distribution, i.e., $(-\frac{4ln(1+\bar{z}^2)(1-\bar{z}^2)}{(1+\bar{r}^2)^2(1+\bar{z}^2)^2})$. When $z = z_m$, this term reduces to zero.

3. Experimental methodology

In this section, the experimental methodology is presented, which was used to assess the ability (or otherwise) of the introduced vortex models to simulate flow and pressure characteristics obtained in a physical tornado-like vortex simulator.
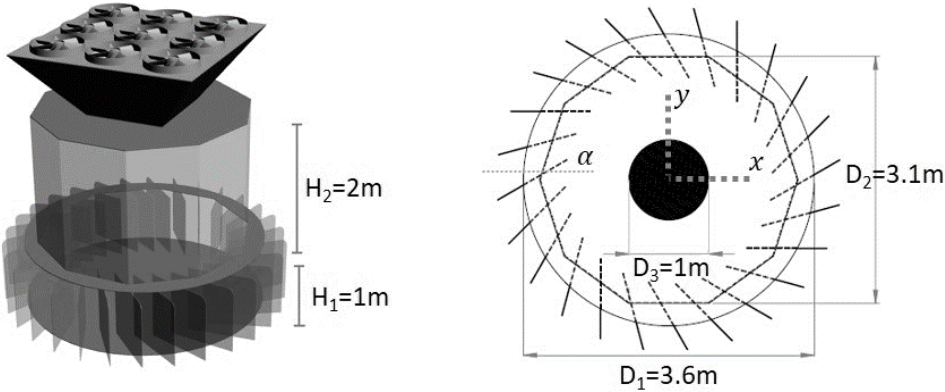
3.1 Tornado-like vortex simulator

For this analysis, the University of Birmingham (UoB) tornado-like vortex generator (3m× 3m), which is based on the design by Ward (1972), is used (Figure 11). The generator consists of two chambers, a convergence chamber with height H_1 and diameter D_1 and a convection chamber with height H_2 and diameter D_2. The aspect ratio (*a*) is defined as the ratio of updraft radius (1/2 D_3) and convergence chamber height and therefore results in an aspect ratio of $a = 2$ for the configuration shown in Figure 11. Angular momentum is introduced by guide vanes around the

594 convergence chamber, which can be set to different angles. By changing the guide vane angle, the
595 vorticity in the flow can be altered and different vortex structures can be generated.
596

597
598 Figure 11: An illustration of the UoB tornado-like vortex generator.
599

600 The kinematic and dynamic similarity of the generated vortex is controlled by the Reynolds
601 number, *Re*, (Eq. *22*) and the swirl ratio, *S*, (Eq. *23*).
602

$$Re = \frac{Q}{\nu \, 0.5 D_3} \tag{22}$$

604

$$S = \frac{tan(\alpha)}{2a} \tag{23}$$

606

607 Here, Q is the flow rate through the simulator and ν is the kinematic viscosity of air. The guide
608 vane angle, α, is the angle relative to the radial velocity component (Figure 11).
609

610 *3.2 Measurement setup and data quality*
611

612 Point velocity measurements were made with 100Hz using a Cobra Probe, which was mounted to
613 a two-axis traverse system inside the simulator. This traverse system enabled the probe to be
614 positioned with an accuracy of 1mm at nine heights (z) above the simulator's surface (0.01m,
615 0.05m, 0.10m, 0.15m, 0.20m, 0.25m, 0.30m, 0.40m, 0.50m, 0.60m) with a radial spacing of
616 0.025m from the centre of the simulator up to a radial distance of 0.60m. The size of the probe is
617 less than 10^6 times smaller than the convergence chamber and the influence of the traverse system
618 on the surface pressure measurements was found to be smaller than the experimental measurement
619 uncertainty. The Cobra Probe can measure velocity data greater than 2m/s within a cone of
620 influence of +/- 45°. These limitations can have a direct influence on the measured data. For
621 example, if the recorded data quality (percentage of velocity samples of a measured time series
622 which are >2m/s and have an angle of attack <+/- 45°) is less than 100% then this can introduce a
623 bias in the calculated velocity vector – the lower the data quality the greater the potential bias. To
624 minimize the bias in time averaged velocities, only those positions with a data quality of greater

625   than 80% were accepted for further analysis. This threshold is assumed to provide a suitable
626   compromise between data quality and quantity.
627
628   The pressure distribution is measured with 100Hz on the ground plane along two perpendicular
629   lines denoted x and y in figure 11. Surface pressure taps are distributed along these lines with a
630   spacing of 0.05m from the simulator's centre up to a distance of 0.75m.
631
632   Different types of uncertainties have to be distinguished. The experimental uncertainty is a
633   combination of uncertainties due to measuring a finite time series (statistical uncertainty), human
634   error such as probe and guide vane angle positioning (repeatability) and the uncertainty of the
635   measurement device itself.
636
637   *3.2.1 Statistical uncertainty*
638
639   The statistical uncertainty is a measure of uncertainty of the time average with respect to the
640   unsteadiness of the flow or surface pressure field. Therefore, it is highly important to verify that
641   the time average of a statistically, stationary stochastic process (such as a tornado) converges
642   against the mean value of all possible realisations within the chosen measurement duration. In
643   order to address the statistical uncertainty for this study, convergence tests were undertaken. For
644   the convergence tests, time series were measured for a duration of 600 seconds. Running averages
645   (*RA*) with increasing sampling durations (from 10 seconds – 600 seconds) were calculated and
646   shown as envelope on the y-axis for the corresponding averaging time. For example, figures 12a
647   and 12b show the convergence tests of the circumferential velocity component and surface
648   pressure at the core radius of the lowest measurement height and at the centre of the simulator,
649   respectively for $S = 0.69$.
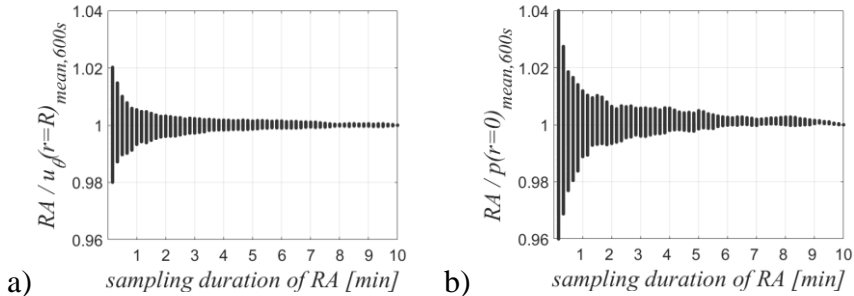
650   a)   b)
651   Figure 12: Convergence test of circumferential velocity (a) and surface pressure (b) for $S = 0.69$.
652
653   Figure 12 indicates that the uncertainty is reduced after a measurement duration of 80 seconds for
654   velocities and 60 seconds for surface pressures. Hence, for this study, velocity and pressure
655   measurements were conducted for a period of 80 and 60 seconds, respectively. The corresponding
656   statistical uncertainties are shown in percentage of the time-average of the corresponding
657   circumferential velocity component ($u_{\theta,mean,600s}$) and surface pressure ($p_{mean,600s}$) which was
658   obtained after sampling for 600 seconds (Table 2).

21

659

660 Table 2: Statistical uncertainties of time-averaged velocity components and surface pressure.

	S = 0.14	*S = 0.30*	*S = 0.69*
	Velocity		
$u_\theta(r=R)_{,mean,600s}$ *[m/s]*	*5.31*	*9.39*	*10.51*
$u_\theta(r=R)_{uncertainty}$ *[%]*	*±1.94*	*±1.02*	*±0.54*
$u_r(r=R)_{uncertainty}$ *[%]*	*±5.96*	*±3.17*	*±0.52*
$w(r=R)_{uncertainty}$ *[%]*	*±1.21*	*±0.55*	*±0.25*
	Pressure		
$p(r=0)_{mean,600s}$ *[Nm^{-2}]*	*-136.30*	*-224.22*	*-164.44*
$p(r=0)_{uncertainty}$ *[%]*	*±26.75*	*±5.94*	*±1.16*

661

662 The 80-second time average of circumferential and vertical velocity components can be
663 determined with an uncertainty of less than ±2% for all swirl ratios. Uncertainties of the radial
664 velocity components are slightly larger with about ±6%, ±3% and ±0.5% for $S = 0.14$, $S = 0.30$
665 and $S = 0.69$, respectively.

666

667 For the surface pressure, 60 seconds of measurement time allow to determine the time-average to
668 about ±27%, ±6% and ±1% for $S = 0.14$, $S = 0.30$ and $S = 0.69$, respectively. The uncertainty of
669 surface pressure measurements at the centre of the simulator seems to be dependent on the swirl
670 ratio, with lower uncertainties with increasing swirl ratio. This could be an indication for a more
671 unstable vortex movement for the lowest swirl ratio compared to larger S. This behaviour cannot
672 be observed in the uncertainties associated with the velocity measurements. A potential reason for
673 this could be that the vortex movement occurs relatively close to the vortex centre where surface
674 pressure gradients are relatively large, especially for the lowest swirl ratio, and for that reason,
675 core radii positions are not that strongly affected by this behaviour.

676

677 *3.2.2 Repeatability*

678

679 The repeatability is the degree to which repeated measurements under unchanged boundary
680 conditions show the same results. Surface pressure measurements and the radial profile of
681 velocities in the lowest measurement height were repeated for five times for each swirl ratio. The
682 measurement repeatability is analysed in form of a distribution of all possible differences of these
683 repetitions. For example, figures 13a and 13b show the measurement repeatability distribution of
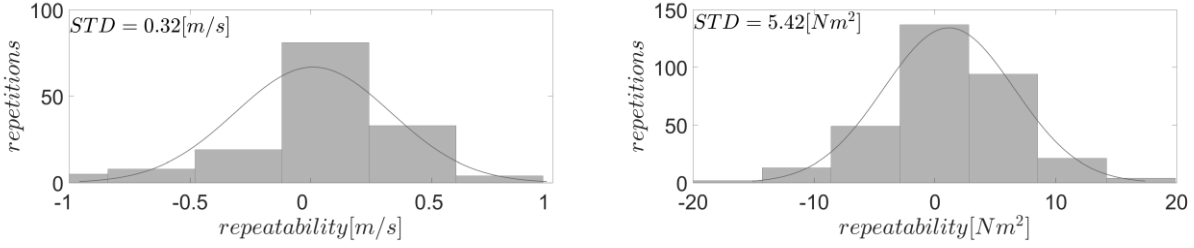684 circumferential velocity component and surface pressure for $S = 0.69$.

Figure 13: Distribution of the repeatability of circumferential velocity component (a) and surface pressure (b) for $S = 0.69$.

The standard deviation (*STD*) of the corresponding distributions was chosen as a representative measure to evaluate the repeatability, which is shown in table 3 for velocity components and surface pressures. Absolute values are given instead of percentages as these uncertainties are assumed to apply for all corresponding time averaged results. Similar to the statistical uncertainty, also table 3 shows that the repeatability of surface pressure measurements is dependent on the swirl ratio. For $S = 0.14$ and $S = 0.30$ the repeatability is not only dependent on the swirl ratio but also on the radial distance. For that reason, a repeatability dependent on r is introduced because a uniform value would highly underestimate the repeatability of measurement positions close to the vortex centre, and highly overestimate the repeatability for positions further away from the vortex centre (Table 3). No significant dependence on the radial distance was found for the repeatability of surface pressure measurements for $S = 0.69$ and all velocity measurements. Consequently, a uniform measurement repeatability independent from r is used for those cases (Table 3).

Table 3: Repeatability of time-averaged velocity components and surface pressures.

	S=0.14	S=0.30	S=0.69
	Velocity		
$u_{\theta,uncertainty}$ [m/s]	±0.51	±0.44	±0.32
$u_{r,uncertainty}$ [m/s]	±0.46	±0.58	±0.22
$W_{uncertainty}$ [m/s]	±0.17	±0.16	±0.08
	$P_{uncertainty}$ [Nm^{-2}]		
-0.05m < r < 0.05m	±53.58	±21.74	±5.42
r = ±0.1m	±12.98	±17.34	±5.42
r > 0.1m & r < -0.1m	±1.86	±3.82	±5.42

The low repeatability close to the vortex centre for $S = 0.14$ and $S = 0.30$ is not too surprising as the statistical uncertainty found at those positions (Table 2) is limiting the repeatability. Therefore, large uncertainties for $S = 0.14$ and $S = 0.30$ close to the vortex core can partly be explained by the large statistical uncertainty at these positions. Furthermore, these findings suggest that especially

23

708 positions close to the centre are sensitive to small variations in the boundary conditions such as
709 guide vane angle positioning.
710
711 *3.2.3 Device uncertainty*
712
713 In this study, pressure transducers (HCLA12X5DB) with a typical uncertainty of ± 5 Nm^{-2} are
714 used. The Cobra Probe is accurate within ± 0.5 m/s for the velocity vector up to a turbulence
715 intensity of ~30%. Therefore, positions with a turbulence intensity greater than 30% are excluded
716 from the analysis. Since the device uncertainty for the Cobra Probe is given for the velocity vector
717 $(\vec{V})$; the uncertainty of each velocity component needs to be calculated for each measurement
718 position based on the obtained average of the corresponding velocity component. Equation 24
719 shows as an example the calculation of the device uncertainty for the circumferential velocity
720 component at a certain position.
721

$$u_{\theta,uncertainty} = 0.5 \ \langle \frac{|u_\theta|}{\vec{V}} \rangle \tag{24}$$

723
724 *3.2.4 Experimental uncertainty*
725
726 The associated experimental uncertainty of velocity and surface pressure measurements, which is
727 shown as envelope in later figures is based on a combination of the repetition uncertainty (shown
728 in table 3) and the device uncertainty.
729
730
731 **4. Comparison**
732
733 In this section, flow field and surface pressure data for three different swirl ratios ($S = 0.14$, $S =$
734 0.30, and $S = 0.69$) are analysed and the capability of the vortex models to replicate the
735 experimental results is evaluated.
736
737 *4.1. The flow structure*
738
739 In order to address the complex nature of the analysed flow fields, the 3-D velocity fields obtained
740 for $S = 0.14$, $S = 0.30$ and $S = 0.69$ are shown in figure 14. Also shown are results of selected
741 analytical vortex models, which for the sake of brevity are not repeated for all swirl ratios. The
742 'viscosity' parameter for the Burgers-Rott and Sullivan model is assumed to be $v=0.05\ m^2s^{-1}$.
743 However, for the analysis presented in figure 14b, the actual 'viscosity' value is not that crucial
744 because the focus of this analysis lies rather on the flow structure than on the actual velocity
745 magnitude, which is affected by the 'viscosity'.
746

747   Velocity components are normalised by the maximum circumferential velocity ($u_{\theta,max}$) of the
748   corresponding swirl ratio. Radial/vertical distances are normalised by the corresponding core
749   radius (R). All of the simplified models presented in section 2 assume a height independent core
750   radius and all vortex models besides the Baker vortex model assume a height independent $u_{\theta,max}$.
751   For this reason, velocity components are normalised by the height average of the maximum
752   circumferential velocity ($u_{\theta,max,average}$) of the corresponding swirl ratio (Eq. 25) and
753   radial/vertical distances are normalised by the corresponding height averaged core radius ($R_{average}$,
754   Eq. 26). The use of averaged quantities is considered to give the best indication of a representative
755   core radius and maximum circumferential velocity for all heights.
756

757
$$u_{\theta,max,average} = \frac{1}{N}\sum_{i=1}^{N} u_{\theta,max}(z)_i \qquad (25)$$

758

759
$$R_{average} = \frac{1}{N}\sum_{i=1}^{N} R(z)_i \qquad (26)$$

760

761   where N is the number of measurement heights.

762

763   A further degree of normalisation is undertaken to aid visual comparisons, i.e., each height (radial
764   distance) is normalised by the corresponding maximum of $z/R_{average}$ ($r/R_{average}$) for each swirl ratio
765   – the actual maxima used are given in the figure captions. Experimentally obtained $R_{average}$ and
766     $u_{\theta,max,average}$ (shown in figure 15) are used to calculate the flow field of the Rankine, Burgers-
767   Rott, Sullivan and Baker vortex models for corresponding swirl ratios. Due to the restrictions when
768   measuring with the Cobra probe, the velocity field close to the vortex centre for all swirl ratios and
769   near the surface at larger radial distances for $S = 0.14$ could not be captured. Inside the vortex core
770   ($r < R_{average}$), velocity vectors are only shown at positions where absolute values of time averaged
771   radial and vertical velocities are larger than the corresponding measurement uncertainty. Hence,
772   only positions for which a clear directionality can be defined are presented in figure 14.

773

774   a₁)   b₁)
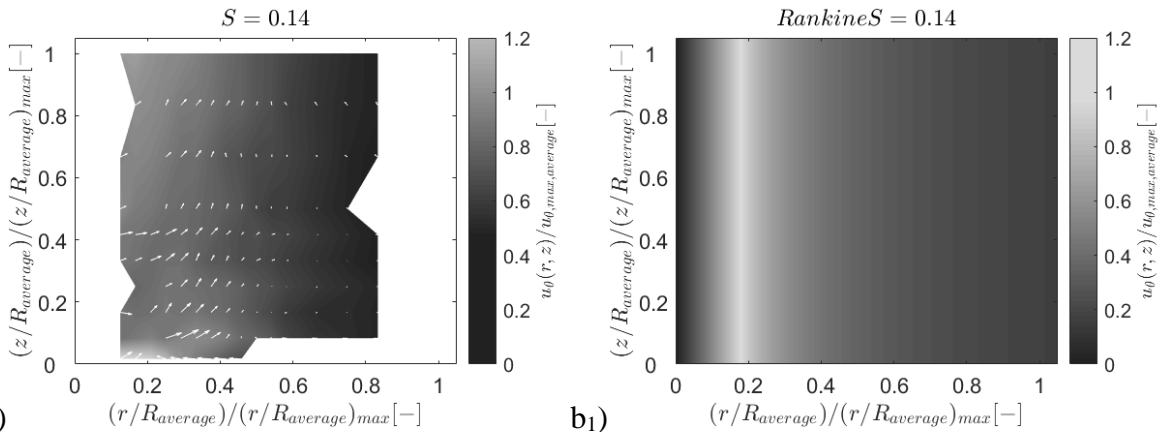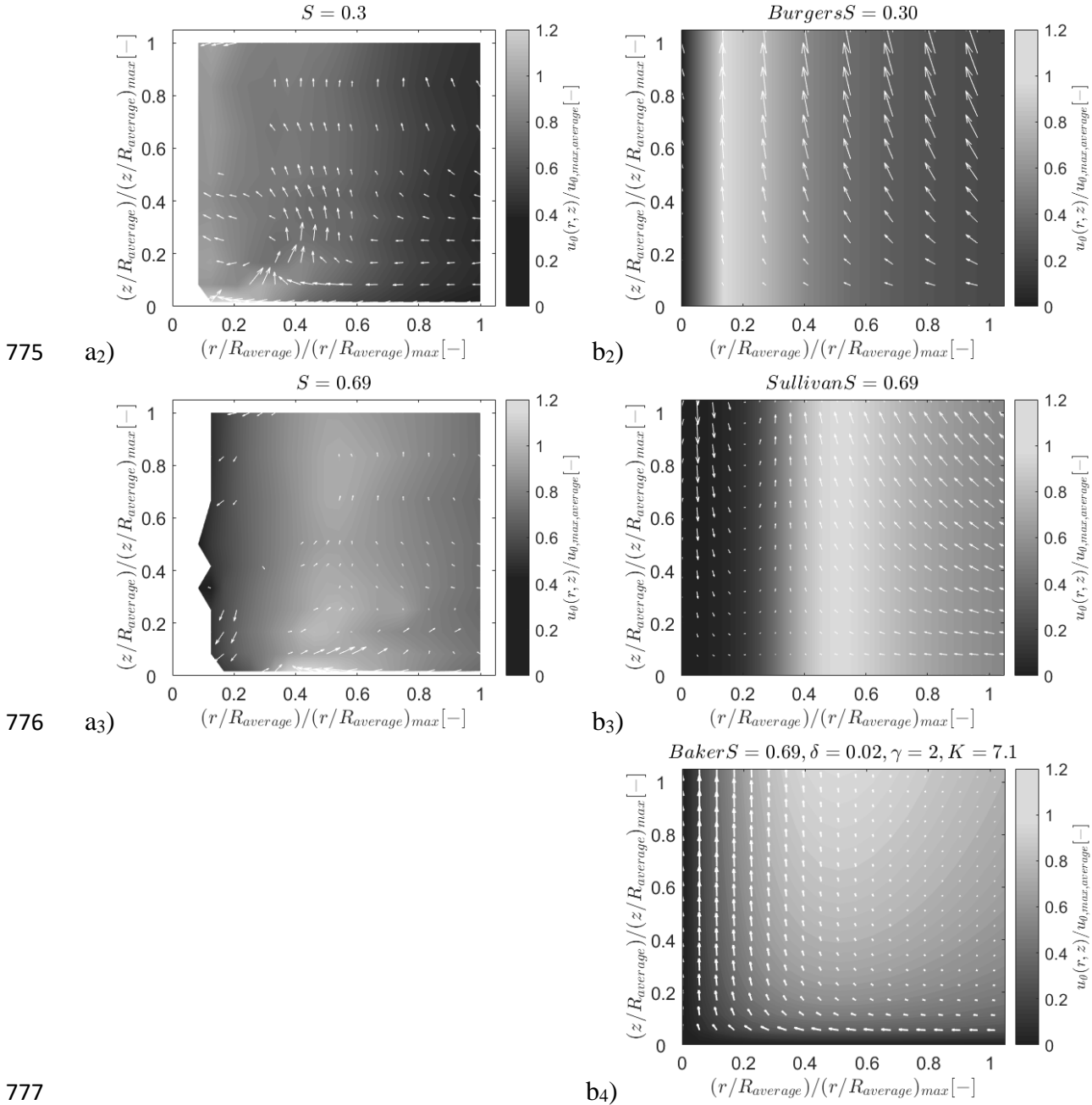
Figure 14: Experimental results of the 3-D velocity field are shown in a_1 ($S = 0.14$), a_2 ($S = 0.30$) and a_3 ($S = 0.69$). Corresponding results of Rankine, Burgers-Rott, Sullivan and Baker vortex models are shown in b_1, b_2, b_3 and b_4, respectively. The normalised circumferential velocity component is shown as contour and radial and vertical velocity components are shown as 2-D vector field. To normalise heights and distances, maximum values of experimentally obtained *(z/R_average) max* and *(r/R_average) max* are used. For $S = 0.14$, $S = 0.30$ and $S = 0.69$ *(r/R_average) max* = *(z/R_average) max* = 5.58, 7.27 and 1.97, respectively.

In general, experimentally obtained flow characteristics reveal much more complex flow patterns compared to the vortex models (Figure 14). The measured circumferential velocity component for all swirl ratios increases towards the core radius and reaches the overall maximum close to the surface. Furthermore, a strong decrease in circumferential velocity can be observed with height in

26

789   the lower heights for all swirl ratios (Figure 14a). The circumferential velocity components of
790   Rankine, Burgers-Rott and Sullivan vortex models (Figure 14b$_1$, Figure 14b$_2$, and Figure 14b$_3$) are
791   not a function of height and consequently, cannot represent the height dependence found in the
792   simulator (Figure 14a). The circumferential velocity of the Baker vortex model is height dependent
793   and increases with increasing height from the ground (Figure 14b$_4$), which is also not obtained
794   experimentally. It can be noticed in figure 14a that for all swirl ratios, a strong inflow can be
795   detected close to the surface, up to the position where the overall maximum circumferential
796   velocity occurs. At this position, the radial velocity drops drastically and the vertical velocity
797   increases significantly.
798
799   Contrary to what may be expected, Figure 14a$_1$, shows a radial outflow from the vortex centre.
800   However, this is supported by the work of Mishra et al., (2008) and Haan et al., (2008), where
801   tentative evidence of a radial outflow close to the vortex centre can be inferred. Various possible
802   reasons for this behaviour (including vortex core unsteadiness with respect to height) could be
803   inferred, however, firm conclusions as to why this may be the case cannot, at present, be drawn.
804
805   With increasing swirl ratio ($S = 0.69$), a downdraft is detected close to the centre of the simulator
806   (Figure 14a$_3$). This flow structure is expected for a two-celled vortex (see Sullivan vortex model,
807   Figure 14c$_3$). However, the downdraft is directed slightly towards the simulator's centre which
808   was also observed by Haan et al., (2008) for a high swirl ratio. The lack of detailed, fine scale,
809   experimental data at the centre of the vortex make further conclusions difficult.
810
811   Due to non-existing radial and vertical velocity components, this behaviour cannot be represented
812   with the Rankine vortex model (Figure 14b$_1$). Notwithstanding the more complex structure of
813   Burgers-Rott, Sullivan, and Baker vortex models, the measured flow pattern are far more complex
814   than the analytical models would suggest.
815
816   A more detailed analysis of the flow field can be found in figures 15 - 17 illustrating the
817   circumferential, radial and vertical velocity components for $z = 0.01$m, $z = 0.10$m, $z = 0.20$m and
818    $z = 0.40$m, for $S = 0.14$ (a), $S = 0.30$ (b) and $S = 0.69$ (c).
819
820   Experimentally obtained results for $\overline{u_\theta}$ (Figure 15) show that for all swirl ratios, the overall
821   maxima of $\overline{u_\theta}$ occurs at the lowest measurement height ($z=0.01$m, Figure 15). The distribution of
822   circumferential velocity components at greater heights is relatively uniform and differences lie
823   within the experimental uncertainty (Figure 15). The lowest height reveals an entirely different
824   flow structure compared to the rest of the generated vortex. This suggests a similar vertical profile
825   of circumferential velocity components as observed by Kosiba and Wurman (2013). Figure 15 also
826   outlines differences in the circumferential velocity profile for different swirl ratios. Figure 15
827   shows that $u_{\theta,max,average}$ increases with increasing swirl ratio from 3.65 – 8.75m/s. Also, the core
828   radius increases with increasing swirl ratio from 0.11 – 0.31m. Results obtained for $S = 0.30$ do

829 not follow this trend and reveal an averaged core radius of 0.08m, which is smaller than the one
830 observed for $S = 0.14$. However, it is worth noting that the difference between $R_{average}$ for $S = 0.14$
831 and $S = 0.30$ is ~0.03m. This difference is within the experimental uncertainty of determining
832 $R_{average}$ and would therefore be masked when taking the uncertainty of determining $R_{average}$ into
833 account, which is approximately $\pm$ 0.02m.
834
835 In general, the Rankine, Burgers-Rott and Sullivan vortex models appear to underestimate the
836 trend of $\overline{u_\theta}$ for $S = 0.14$ (Figure 15a), although the differences are close to or within the
837 experimental uncertainty in most cases. However, the Baker model appears to predict the trend
838 reasonably well for this swirl ratio. All models appear to fail to capture the distribution of $\overline{u_\theta}$ at
839 relatively large values of S (Figure 15b).
840
841 Inside the vortex core, a comparison between experimentally obtained results and vortex models
842 is difficult due to the lack of good experimental data for $S = 0.14$ and $S = 0.30$ (Figure 15a and
843 Figure 15b). The circumferential velocity component of the Burgers-Rott and Baker vortex model
844 match the experimental data obtained for $S = 0.69$ (Figure 15c). Results from the Rankine and
845 Sullivan vortex model, again underestimate the magnitude of obtained circumferential velocities
846 for the highest swirl ratio.

847 a)

848 b)
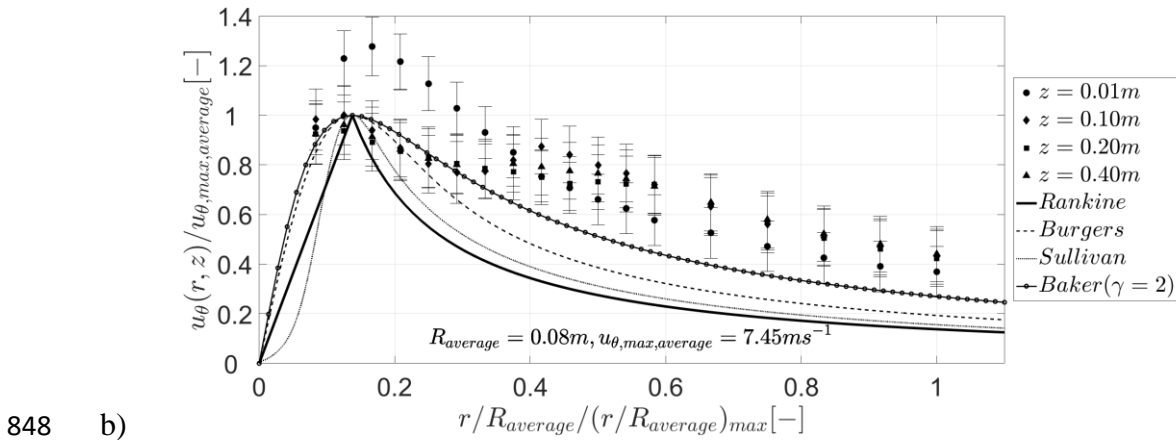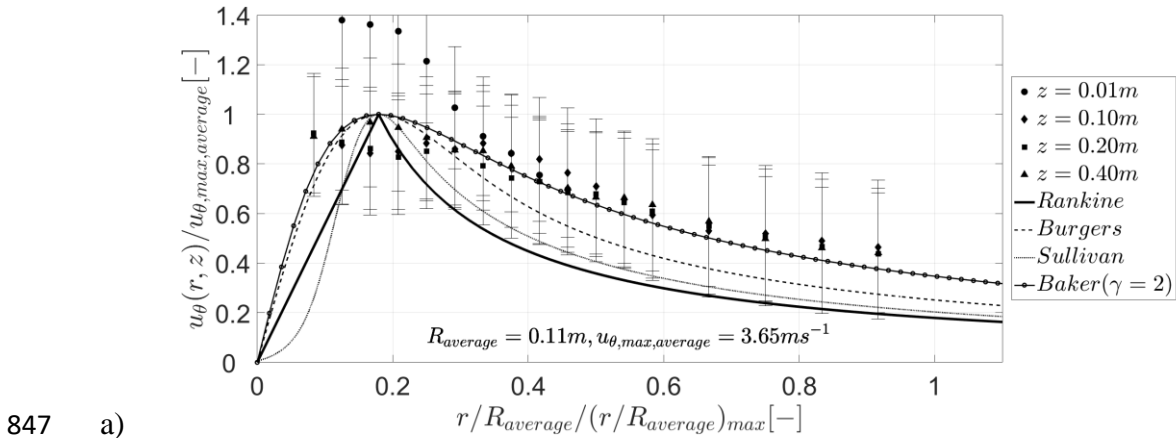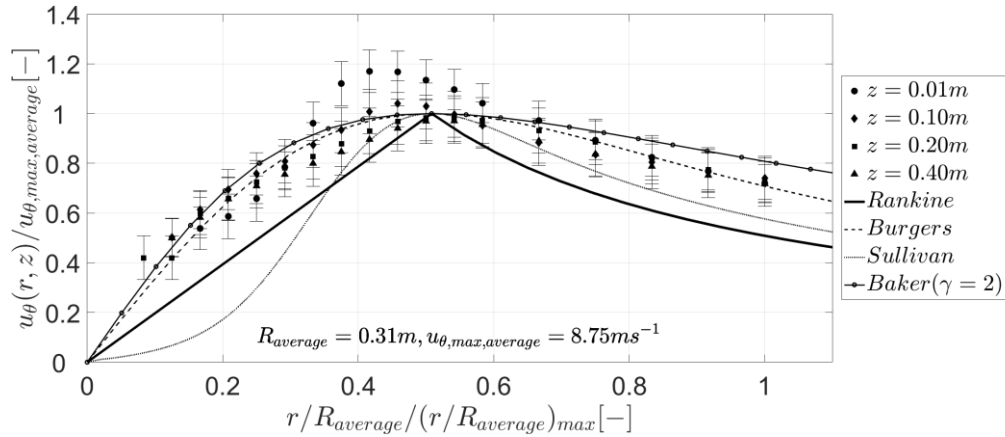
849　c)

Figure 15: Measured circumferential velocity component for $S = 0.14$ (a), $S = 0.30$ (b) and $S = 0.69$ (c). Additionally, results of the circumferential velocity component of Rankine, Burgers-Rott, Sullivan, and Baker vortex models are shown. To normalise the radial distance, maximum values of experimentally obtained *(r/R$_{average}$)* $_{max}$ are used. For $S = 0.14$, $S = 0.30$ and $S = 0.69$ *(r/R$_{average}$) $_{max}$ = (z/R$_{average}$) $_{max}$* = 5.58, 7.27 and 1.97, respectively.

Figure 16 illustrates the radial distribution of $\overline{u_r}$ for $z = 0.01$m, $z = 0.10$m, $z = 0.20$m and $z = 0.40$m. Additionally a height average is calculated and shown for all velocities obtained for $z > 0.01$m. It needs to be mentioned here that the swirl ratio (S) defined in equation *23* is, unlike the definition adopted in the Baker vortex model (S_{Baker}), solely a function of the tornado generator characteristics. For that reason, values of S and S_{Baker} differ for the same flow field in the following figures. As illustrated in figure 16a and 16b, the Baker model fits the data obtained reasonably well close to the surface, whereas the Sullivan and Burgers-Rott vortex model are a better fit for experimental data obtained in greater heights. This is perhaps not too surprising given the assumptions embedded in the models. However, for the largest swirl ratio (Figure 16c), the Baker model only represents the trend in the lowest height for normalised radial distances greater than 0.6, whereas the Sullivan model performs better for the lowest height and for lower normalised radial distances.

For *S = 0.14*, the radial outflow inside the vortex core suggests the structure of a (limited height) two-celled vortex. Thus, in general, the height averaged structure of $\overline{u_r}$ appears to be reasonably represented by the Sullivan vortex model (Figure 16a). Even though one feature of a two-celled vortex is present for *S = 0.14*, the vertical downdraft suggested by the Sullivan vortex model at the vortex centre was not capture (Figure 17a). For the vertical velocity component obtained with $S = 0.14$, none of the vortex models is capable of replicating the maximum updraft just outside the vortex core (Figure 17a). However, for larger radial distances, results of Burgers-Rott and Sullivan vortex model can be used to reproduce height averaged vertical velocities (Figure 17a). Certainly, it needs to be mentioned here that for this case, the vortex models fail to replicate the complex behaviour observed experimentally. Although there are only few positions available for a comparison in the lowest height, radial and vertical velocity component of the Baker vortex model are in good agreement with the experimental data (Figure 16a and Figure 17a).

29

880

881   For $S = 0.30$, radial velocities are mainly directed towards the vortex centre (radial inflow). The
882   magnitude of radial velocities in greater heights z > 0.01m is relatively low compared to radial
883   velocities obtained in the lowest height (*z=0.01m*). The best fit for this 'single-celled' flow
884   behaviour is achieved with the Burgers-Rott vortex model with a relatively low 'viscosity'
885   parameter (*v=0.0015m²s⁻¹*) to minimise the increase of radial inflow from the vortex centre to
886   larger radial distances. Similar to the vertical velocity component found for $S = 0.14$, also here the
887   maximum updraft outside the vortex core (Figure 17b) cannot be replicated by any of the
888   introduced vortex models. However, for larger radial distances the Burgers-Rott vortex model can
889   be used to model the height averaged behaviour (Figure 17b). Nevertheless, the complex vertical
890   flow structure cannot be captured. Radial and vertical velocity component of the Baker vortex
891   model on the other hand are in good agreement with the experimental data for *z=0.01m* (Figure
892   16b and Figure 17b).

893

894   For $S = 0.69$, radial velocities (Figure 16c) are found to be directed inwards, towards the vortex
895   centre (radial inflow), even though a downdraft close to the vortex centre is found (Figure 17c). In
896   terms of vortex models, this means that the radial velocity shows a 'single-celled' behaviour with
897   radial inflow (Burgers-Rott and Baker), whereas the vertical velocity illustrates a 'two-celled'
898   structure with downdraft (Sullivan). None of the presented vortex models is capable of
899   representing both of the observed flow patterns. For $S = 0.69$, the flow field obtained is far more
900   complex than the assumed flow structure of a single or a double-celled vortex. In this case, the
901   flow reveals a 'multi-celled' structure with a weak radial inflow and updraft outside the core vortex
902   and relatively strong radial inflow and downdraft inside the core vortex (Figure 16c and Figure
903   17c).

904

905   For radial and vertical velocity components of $S = 0.69$, an attempt is shown to use Sullivan and
906   Baker vortex model to replicate some of the flow patterns observed in the lowest height (z =
907   0.01m). For the radial velocity component in the lowest height (Figure 16c), the Baker vortex
908   model captures the radial inflow outside the vortex core but overestimates velocities inside the
909   vortex core. The decrease in radial inflow around the core radius can be replicated with the Sullivan
910   vortex model, however, close to the vortex centre, the Sullivan vortex model is not able to replicate
911   the flow field and also for larger radial distances the Sullivan vortex model fails due to its
912   increasing radial velocity component with increasing radial distance (Figure 16c).

913

914   For the vertical velocity (Figure 17c), the Sullivan vortex model can represent parts of the observed
915   results. By means of the shape parameter, *b*, the downdraft region around the vortex centre of the
916   Sullivan vortex model can be extended in the radial direction so that for *b = 12*, results of the
917   Sullivan model show some similarity with the increase in radial inflow from the vortex core
918   towards the vortex centre (Figure 17c). However, increasing, *b*, also results in an increasing
919   downdraft at the core radius, which for $S = 0.69$ is highly overestimated. The Baker vortex model
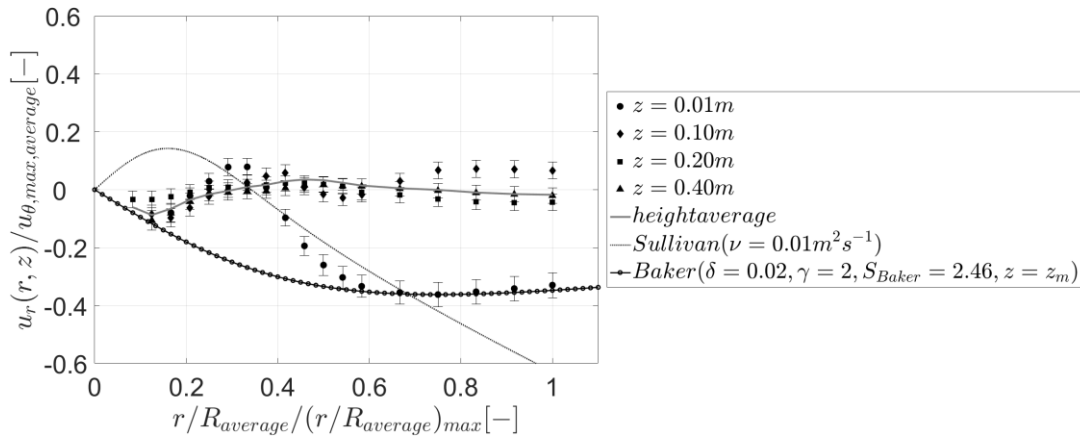
920 is not able to replicate the downdraft close to the vortex centre and the relatively strong vertical
921 updraft around the core radius.
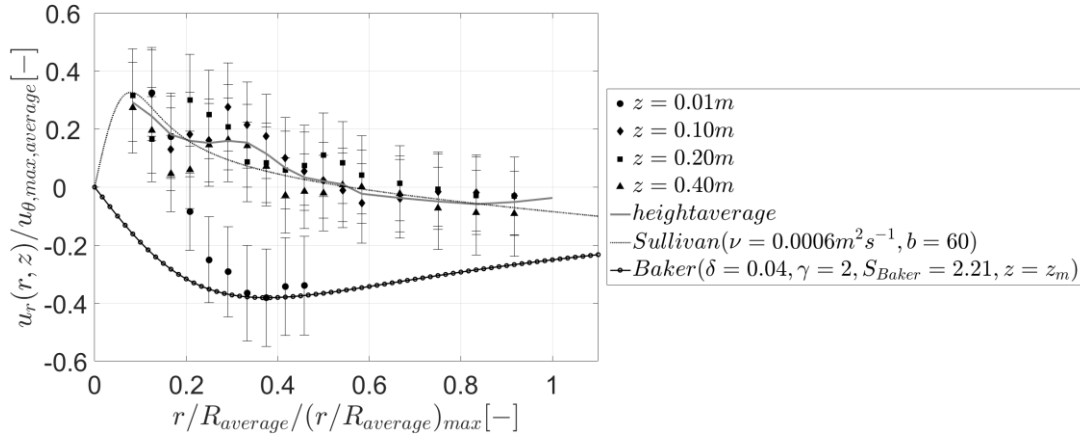
922 a)
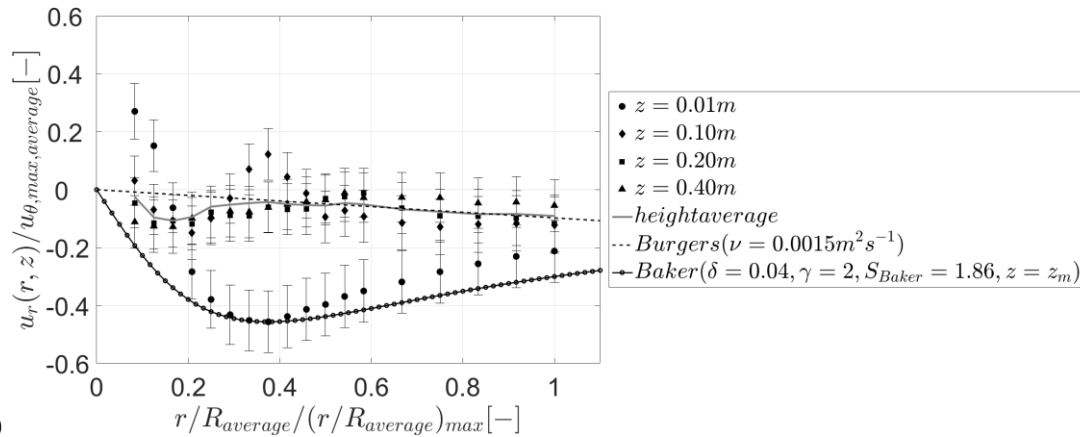
923 b)

924 c)

925 Figure 16: Measured radial velocity component for *S* = 0.14 (a), *S* = 0.30 (b) and *S* = 0.69 (c). Additionally, results
926 of the radial velocity component of Burgers-Rott (b) and Sullivan vortex model (a and c) are shown. Results of the
927 Baker vortex model are shown for the lowest height ($z = 0.01$). To normalise the radial distance, maximum values of
928 experimentally obtained *(r/R_average) max* are used. For *S* = 0.14, *S* = 0.30 and *S* = 0.69 *(r/R_average) max* = *(z/R_average) max* =
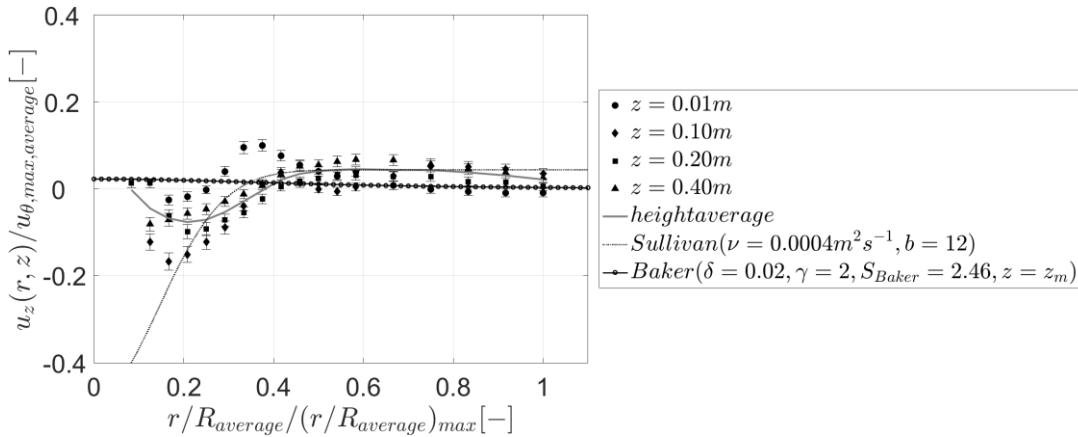929 5.58, 7.27 and 1.97, respectively.
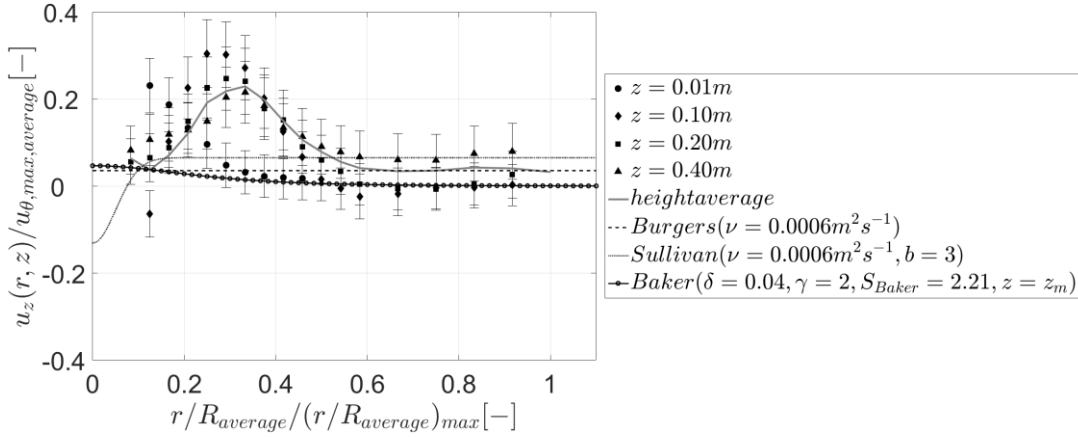
930   a)
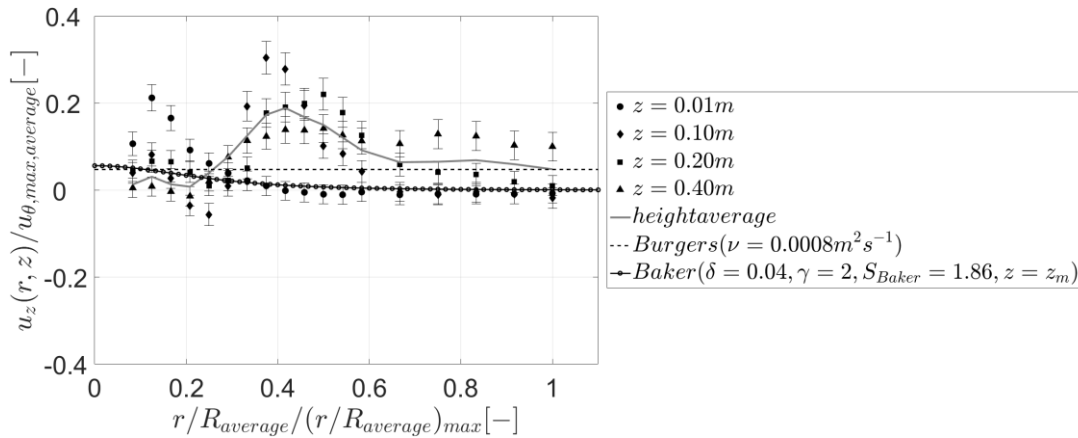
931   b)

932   c)

Figure 17: Measured vertical velocity component for *S* = 0.14 (a), *S* = 0.30 (b) and *S* = 0.69 (c). Additionally, results of the vertical velocity component of Burgers-Rott (a and b) and Sullivan vortex model (a and b) are shown. Results of the Baker vortex model are shown for the lowest height (z = 0.01). To normalise the radial distance, maximum values of experimentally obtained *(r/R_{average}) _{max}* are used. For *S* = 0.14, *S* = 0.30 and *S* = 0.69 *(r/R_{average}) _{max}* = *(z/R_{average}) _{max}* = 5.58, 7.27 and 1.97, respectively.

4.2 Surface pressure distribution

941   Figure 18 and figure 19 show the surface pressure distribution for $S = 0.14$, $S = 0.30$, and $S = 0.69$.
942   Additionally, the surface pressure distributions of the Rankine, Burgers-Rott and Sullivan vortex
943   models are illustrated in figure 18 and results of the Baker vortex model are shown in figure 19.
944
945   Looking at figures 18 and 19, it could be concluded that differences in the measured surface
946   pressure distribution depend significantly on the swirl ratio. As expected, the smallest vortex
947   shows the fastest increase in surface pressure from the vortex centre towards larger radial distances
948   ($S = 0.14$). The slope of the surface pressure change is determined by the measured surface
949   pressure distribution but also affected by the normalisation of radial distances. This means, for the
950   same surface pressure distribution, a larger core radius leads to a surface pressure distribution,
951   which is increasing faster from the vortex centre towards larger radial distances. For that reason,
952   the surface pressure distribution of $S = 0.30$ and $S = 0.60$ reveal an unexpected behaviour. The
953   surface pressure distribution obtained with $S = 0.69$ displays a faster increase of surface pressure
954   with increasing radial distance compared to the pressure distribution measured with $S = 0.30$. This
955   can be explained by the relatively small averaged core radius for $S = 0.30$ ($R_{average, (S=0.30)} = 0.08$m)
956   compared to $R_{average}$ of $S = 0.14$ ($R_{average, (S=0.14)} = 0.11$m) and $S = 0.69$ ($R_{average, (S=0.69)} = 0.31$m).
957
958   To avoid an unphysical decrease in surface pressure with increasing radial distance, the 'viscosity'
959   parameter of the Sullivan vortex model is chosen to be zero and for the Burgers-Rott vortex model,
960   v and $\bar{a}$ are adjusted for each swirl ratio to guaranty a physically reasonable surface pressure
961   increase with increasing radial distance (Figure 18).
962
963   The largest differences in the surface pressure distribution of the vortex models is found close to
964   the vortex centre, whereas largest differences in the experimental surface pressure data for the
965   three different vortices are found outside the vortex core (Figure 18). The surface pressure
966   distributions of the Rankine and Burgers-Rott vortex models are in good agreement with the
967   experimental data for $S = 0.69$ (Figure 18), albeit the Burgers-Rott vortex model fails for larger
968   radial distances due to a physically unrealistic decrease in surface pressure, which is explained in
969   section 2.8. Also, the Sullivan vortex model shows good agreement for this swirl ratio ($S = 0.69$)
970   but only for larger radial distances. Close to the vortex centre, the Sullivan vortex model
971   underestimates experimental results due to its two-celled structure (Figure 18). Even though a
972   downdraft is present close to the vortex centre for $S = 0.69$, the effect of it is not visible in the
973   experimentally obtained surface pressure distribution.
974
975   All three solutions of the Baker vortex model match the experimental surface pressure for $S = 0.30$
976   the best (Figure 19). The swirl ratio of the Baker vortex model (S_{Baker}) is responsible for differences
977   in the surface pressure distribution. However, differences in S_{Baker} for the three analysed vortices
978   are too small to cause significant differences in the surface pressure distribution (Figure 19). To
979   allow a more flexible surface pressure model, the shape parameter, γ, in the Baker model needs to
980   be treated as a variable when deriving the static pressure distribution (Eq. 19). This would allow

981 different core radii (R_{Baker}) and also different shapes of the surface pressure distribution to be
982 generated. However, in this work, the surface pressure equation for the Baker vortex model (Eq.
983 19) assumes a shape parameter of *γ=2*. Consequently, the calculated surface pressure distributions
984 shown in figure 19 assume a constant core radius (R_{Baker}) for all three vortices. For this reason, the
985 surface pressure distributions of the Baker vortex model does not allow an accurate representation
986 of the experimentally obtained surface pressure profiles.
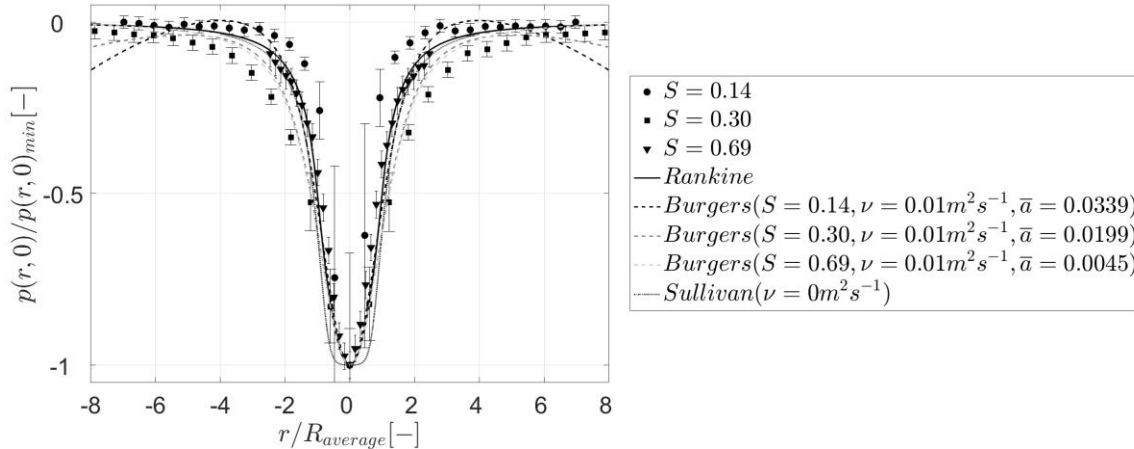
987
988 Figure 18: Measured surface pressure distribution for S=0.14 (a), S=0.30 (b), and S=0.69 (c) and surface pressure of
989 Rankine, Burgers-Rott, and Sullivan vortex model.
990
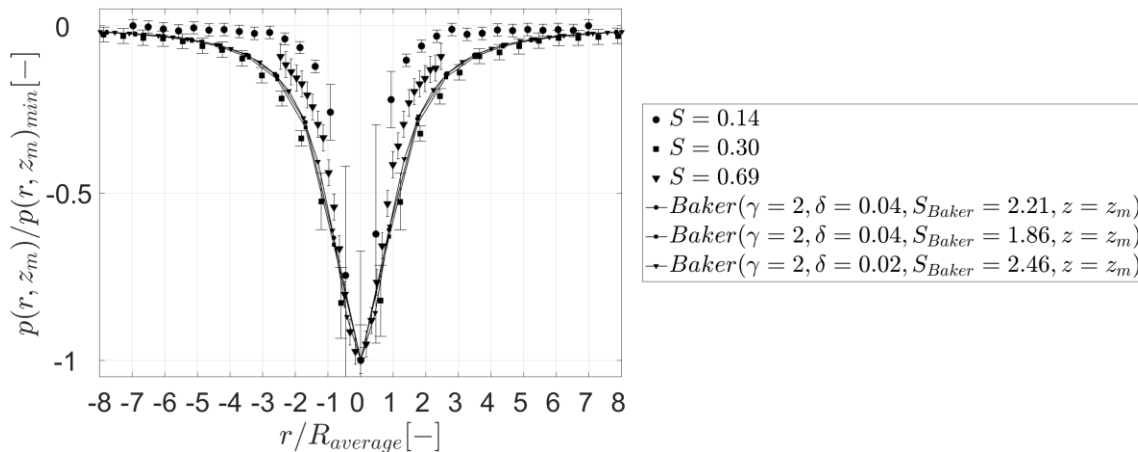
991
992 Figure 19: Measured surface pressure distribution for S=0.14 (a), S=0.30 (b), and S=0.69 (c) and surface pressure of
993 the Baker vortex model.
994
995
996 **5. Conclusion**
997
998 Based on this analysis, the following main conclusions can be drawn:
999

34

- Despite the simplicity of all the models examined, it has been shown that this area of research is highly complex, largely due to the interpretation of the different parameters involved.
- The Burgers-Rott and Sullivan vortex models are able to replicate some parts of the flow field. However, parameters, which need to be chosen to make the model results fit the experimental data (ν, $\bar{a}$ and b) differ for surface pressure and different velocity components of the same vortex.
- The Baker vortex model seemed to be the best model to replicate the radial inflow close to the ground. However, it fails for larger heights over the range tested.
- Measured flow pattern are far less structured and organised than the pattern suggested by any of the vortex models. Consequently, none of the presented models can be used to represent the three dimensional vortex structures of experimentally generated tornado-like vortices.
- Rankine, Burgers-Rott and Sullivan vortex model are able to replicate the surface pressure distribution of one of the analysed vortices ($S = 0.69$) but due to their limitations, these models are not adequate enough to replicate a variety of differently shaped pressure distributions.
- The Baker vortex model with a shape parameter of $\gamma = 2$ allows the representation of the surface pressure distribution obtained for ($S = 0.30$). A more general expression for the surface pressure is required to represent experimental data for all three vortices.

References

Alekseenko, S.V., Kuibin, P.A., Okulov, V.L., 2007. Theory of Concentrated Vortices. Springer Berlin Heidelberg New York. ISBN 978-3-540-73376-8. http://doi.org/10.1007/978-3-540-73376-8

Alexander, C.R. and Wurman J.M., 2008. Updated mobile radar climatology of supercell tornado structures and dynamics. 24th Conference on Severe Local Storms, Savannah, GA.

Baker C.J. and Sterling M., 2017. Modelling wind fields and debris flight in tornadoes. Journal of Wind Engineering and Industrial Aerodynamics 168, 312-321. https://doi.org/10.1016/j.jweia.2017.06.017

Batterson J.W., Maicke B.A., Majdalani J., 2007. Advancements in Theoretical Models of Confined Vortex Flowfields. Defense Technical Information Center, University of Tennessee Space Institute, Tullahoma, TN 37388.

Bech J., Gayà M., Aran M., Figuerola F., Amaro J., Arús J., 2009. Tornado damage analysis of a forest area using site survey observations, radar data and a simple analytical vortex model. Atmospheric Research 93, 118–130. https://doi.org/10.1016/j.atmosres.2008.10.016

Bloor, M.I.G., Ingham, D.B., 1987. The flow in industrial cyclones. Journal of Fluid Mechanics 178, 507-519. https://doi.org/10.1017/S0022112087001344

Brown, R.A., Wood, V.T., 2004. Comparisons of Doppler velocity tornadic vortex signatures with signatures from model vortices. 22nd Conference on Severe Local Storms, Anonymous Hyannis, MA.

1046	*Burgers, J.M., 1948. A Mathematical Model Illustrating the Theory of Turbulence. Advances in Applied Mechanics*
1047	*1, 171-199. https://doi.org/10.1016/S0065-2156(08)70100-5*
1048
1049	*Church, C.R., Snow, J.T., Baker, G.L., Agee, E.M., 1979. Characteristics of Tornado-Like Vortices as a Function of*
1050	*Swirl Ratio: A Laboratory Investigation. Journal of the Atmospheric Sciences 36, 1755-1776.*
1051	*https://doi.org/10.1175/1520-0469(1979)036<1755:COTLVA>2.0.CO;2*
1052
1053	*Davies-Jones, R. and Kessler, E., 1974. Tornadoes. Weather and Climate Modification, W. N. Hess, Ed., Wiley, 552-*
1054	*595.*
1055
1056	*Davies-Jones, R., Trapp, R.J., Bluestein, H.B., 2001. Tornadoes and Tornadic Storms. Meteorological Monographs*
1057	*50, 167-222. https://doi.org/10.1175/0065-9401-28.50.167*
1058
1059	*Gillmeier, S., Sterling, M., Hemida, H., 2016. An Analysis of the Influence of a Tornado Generator's Geometry on*
1060	*the Flow Field. 8th International Colloquium on Bluff Body Aerodynamics and Applications. Boston, Massachusetts,*
1061	*USA.*
1062
1063	*Haan Jr, F.L., Sarkar, P.P., Gallus, W.A., 2008. Design, construction and performance of a large tornado simulator*
1064	*for wind engineering applications. Engineering Structures 30, 1146-1159.*
1065	*https://doi.org/10.1016/j.engstruct.2007.07.010*
1066
1067	*Hashemi Tari, P., Gurka, R., Hangan, H., 2010. Experimental investigation of tornado-like vortex dynamics with*
1068	*swirl ratio: The mean and turbulent flow fields. Journal of Wind Engineering and Industrial Aerodynamics 98, 936-*
1069	*944. https://doi.org/10.1016/j.jweia.2010.10.001*
1070
1071	*Hoecker, W.H., 1960. Wind speed and air flow patterns in the Dallas tornado of April 2, 1957. Monthly Weather*
1072	*Review 88, 167-180. https://doi.org/10.1175/1520-0493(1960)088<0167:WSAAFP>2.0.CO;2*
1073
1074	*Karstens, C.D., Samaras, T.M., Lee, B.D., Gallus Jr., W.A., Finley, C.A., 2010. Near-Ground Pressure and Wind*
1075	*Measurements in Tornadoes. Monthly Weather Review 138, 2570-2588. https://doi.org/10.1175/2010MWR3201.1*
1076
1077	*Kilty, K.T., 2005. Steady-state tornado vortex models. http://www.kilty.com/pdfs/models.pdf (last accessed*
1078	*08/06/2017).*
1079
1080	*Kim, Y.C., Matsui, M., 2017. Analytical and empirical models of tornado vortices: A comparative study. Journal of*
1081	*Wind Engineering and Industrial Aerodynamics 171, 230-247. https://doi.org/10.1016/j.jweia.2017.10.009*
1082
1083	*Kosiba, K., Wurman, J., 2010. The Three-Dimensional Axisymmetric Wind Field Structure of the Spencer, South*
1084	*Dakota, 1998 Tornado. Journal of the Atmospheric Sciences 67, 3074-3083. https://doi.org/10.1175/2010JAS3416.1*
1085
1086	*Kosiba, K., Wurman, J., 2013. The Three-Dimensional Structure and Evolution of a Tornado Boundary Layer.*
1087	*Weather and Forecasting 28, 1552-1561. https://doi.org/10.1175/WAF-D-13-00070.1*
1088
1089	*Kuo, H.L., 1971. Axisymmetric Flows in the Boundary Layer of a Maintained Vortex. Journal of the Atmospheric*
1090	*Sciences 28, 20-41. https://doi.org/10.1175/1520-0469(1971)028<0020:AFITBL>2.0.CO;2*
1091
1092	*Lee, J., Samaras, T., Young, C. R., 2004. Pressure measurements at the ground in an F-4 tornado. 22nd Conference*
1093	*on Severe Local Storms, Anonymous Hyannis, MA.*
1094
1095	*Lewellen, W.S., 1993. Tornado Vortex Theory, The Tornado: Its Structure, Dynamics, Prediction, and Hazards.*
1096	*Geophys. Monogr 79, edited by C. Church et al., pp. 19-39, AGU, Washington, D. C. https://doi.org/*
1097	*10.1029/GM079*
1098
1099	*Lewellen, W.S., Lewellen, D.C., Sykes, R.I., 1997. Large-Eddy Simulation of a Tornado's Interaction with the*
1100	*Surface. Journal of the Atmospheric Sciences 54, 581-605. https://doi.org/10.1175/1520-*
1101	*0469(1997)054<0581:LESOAT>2.0.CO;2*

Liu, Z., Ishihara, T., 2016. Study of the effects of translation and roughness on tornado-like vortices by large-eddy simulations. Journal of Wind Engineering and Industrial Aerodynamics 151, 1-24. https://doi.org/10.1016/j.jweia.2016.01.006

Mishra, A.R., James, D.L., Letchford, C.W., 2008. Physical simulation of a single-celled tornado-like vortex, Part A: Flow field characterization. Journal of Wind Engineering and Industrial Aerodynamics 96, 1243-1257. https://doi.org/10.1016/j.jweia.2008.02.063

Natarajan, D., 2011. Numerical Simulation of Tornado-like Vortices. The University of Western Ontario Electronic Thesis and Dissertation Repository.

Natarajan, D., Hangan H., 2012. Large eddy simulations of translation and surface roughness effects on tornado-like vortices. Journal of Wind Engineering and Industrial Aerodynamics 104-106, 577-584. https://doi.org/10.1016/j.jweia.2012.05.004

Nolan, D.S., Dahl, N.A., Bryan, G.H., Rotunno, R., 2017. Tornado Vortex Structure, Intensity, and Surface Wind Gusts in Large-Eddy Simulations with Fully Developed Turbulence. Journal of the Atmospheric Sciences 74, 1573-1597. https://doi.org/10.1175/JAS-D-16-0258.1

Rankine, W.J.M., 1882. A Manual of Applied Physics. 10th ed. Charles Griff and Co. 663 pp.

Refan, M., Hangan, H., 2016. Characterization of tornado-like flow fields in a new model scale wind testing chamber. Journal of Wind Engineering and Industrial Aerodynamics 151, 107-121. https://doi.org/10.1016/j.jweia.2016.02.002

Refan, M., Hangan, H., Wurman, J., 2014. Reproducing tornadoes in laboratory using proper scaling. Journal of Wind Engineering and Industrial Aerodynamics 135, 136-148. https://doi.org/10.1016/j.jweia.2014.10.008

Refan, M., Hangan, H., Wurman, J., Kosiba, K., 2017. Doppler radar-derived wind field of five tornado events with application to engineering simulations. Engineering Structures 148, 509-521. https://doi.org/10.1016/j.engstruct.2017.06.068

Rott, N., 1958. On the viscous core of a line vortex. Zeitschrift für angewandte Mathematik und Physik ZAMP 9, 543-553. https://doi.org/10.1007/BF02424773

Sabareesh, G.R., Matsui, M., Tamura, Y., 2012. Dependence of surface pressures on a cubic building in tornado like flow on building location and ground roughness. Journal of Wind Engineering and Industrial Aerodynamics 103, 50-59. https://doi.org/10.1016/j.jweia.2012.02.011

Sullivan, R.D., 1959. A Two-Cell Vortex Solution of the Navier-Stokes Equations. Journal of the Aerospace Sciences 26, 767-768. https://doi.org/10.2514/8.8303

Tang, Z., Feng, C., Wu, L., Zuo, D., James, D.L., 2017. Characteristics of Tornado-Like Vortices Simulated in a Large-Scale Ward-Type Simulator. Boundary-Layer Meteorology, 1-24. https://doi.org /10.1007/s10546-017-0305-7

Trapp R.J., 2000. A Clarification of Vortex Breakdown and Tornadogenesis. Monthly Weather Review 128, 888-895. https://doi.org/10.1175/1520-0493(2000)128<0888:ACOVBA>2.0.CO;2

Vatistas, G.H., Kozel V. and Mih, W.C., 1991. A simpler model for concentrated vortices. Experiments in Fluids, 11, 73–76. https://doi.org/10.1007/BF00198434

Vyas, A. B., Majdalani, J., and Chiaverini, M. J., 2003. The Bidirectional Vortex. Part 1: An Exact Inviscid Solution. AIAA 2003-5052. https://doi.org/10.2514/6.2003-5052

1158   *Ward, N.B., 1972. The Exploration of Certain Features of Tornado Dynamics Using a Laboratory Model. Journal of*
1159   *the Atmospheric Sciences 29, 1194-1204. https://doi.org/10.1175/1520-0469(1972)029<1194:TEOCFO>2.0.CO;2*
1160
1161   *Winn, W.P., Hunyady, S.J., Aulich, G.D., 1999. Pressure at the ground in a large tornado. Journal of Geophysical*
1162   *Research: Atmospheres 104, 22067-22082. https://doi.org/10.1029/1999JD900387*
1163
1164   *Wood, V.T., Brown, R.A., 2011. Simulated Tornadic Vortex Signatures of Tornado-Like Vortices Having One- and*
1165   *Two-Celled Structures. Journal of Applied Meteorology and Climatology 50, 2338-2342.*
1166   *https://doi.org/10.1175/JAMC-D-11-0118.1*
1167
1168   *Wood, V.T., White, L.W., 2011. A New Parametric Model of Vortex Tangential-Wind Profiles: Development,*
1169   *Testing, and Verification. Journal of the Atmospheric Sciences 68, 990-1006.*
1170   *https://doi.org/10.1175/2011JAS3588.1*
1171
1172   *Wurman, J., Gill, S., 2000. Finescale Radar Observations of the Dimmitt, Texas (2 June 1995), Tornado. Monthly*
1173   *Weather Review 128, 2135-2164. https://doi.org/10.1175/1520-0493(2000)128<2135:FROOTD>2.0.CO;2*
1174
1175   *Wurman, J., Kosiba, K., Robinson, P., 2013. In Situ, Doppler Radar, and Video Observations of the Interior*
1176   *Structure of a Tornado and the Wind–Damage Relationship. Bulletin of the American Meteorological Society 94,*
1177   *835-846. https://doi.org/10.1175/BAMS-D-12-00114.1*
1178
1179   *Xu, Z and Hangan, H., 2009. An Inviscid Solution for Modeling of Tornadolike Vortices. Journal of Applied*
1180   *Mechanics 76, 031011-031011-031015. https://doi.org/10.1115/1.3063632*